Generalized lattice Boltzmann method for radiative transfer problem in slab and irregular graded-index media

Guillaume Lambou Ymeli [*]

Unité de Recherche de Mécanique et de Modélisation des Systèmes Physiques (UR2MSP), Department of Physics, University of Dschang, Cameroon

Cun-Hai Wang [†]

School of Energy and Environmental Engineering, University of Science and Technology Beijing, Beijing 100083, China

The lattice Boltzmann method (LBM) has been developed as a powerful solution method in computational fluid dynamics and heat transfer. However, the development of the LBM for solving radiative transfer problems has been far from perfect. This paper proposes a generalized form of the lattice Boltzmann model for the multidimensional radiative transfer equation (RTE) in irregular geometry with a graded index based on body-fitted coordinates. The macroscopic RTE is recovered from Chapman-Enskog analysis, which provides two possible procedures to formulate the Boltzmann equation in graded-index media and irregular geometries. These proposed models have been tested by considering one-and two-dimensional problems of the RTE, and the benchmark solutions reported in the literature were used for comparisons. Afterwards, the LBM is used to analyze the radiation transport in graded-index media for various forms of scattering law, refractive index, boundary reflection, laser and optical properties, and temperatures. The graded-index function and the geometry type have a significant effect on radiative transport in cases in which the refractive index matches or mismatches the boundary. It is also apparent that the developed LBM is an efficient, powerful, robust, and accurate solver for radiative transport in inhomogeneous media with a graded-index function and irregular geometries.

I. INTRODUCTION

Several generations of researchers in the radiative transfer community have studied the problem of radiative transfer through participating media. This particular interest can be justified by the fact that radiations play an important role in many applications, such as the interpretation of spectroscopic emissions from stars, planets, and atmosphere [1–3], nuclear engineering [4–6], biological tissues [7], thermal insulations [8], and glass fabrication and combustion systems [9,10]. Radiative transfer in such problems can accurately be predicted through the radiative transfer equation (RTE) solution. The RTE is an integrodifferential equation of seven variables: three spatial coordinates, a polar and an azimuthal angle, time, and spectral dimension. Therefore, an accurate, simple, and efficient tool to solve the radiative transfer problem is required for these applications. In addition to its dependence on spatial and angular variables, the ray goes along a curved path that is clearly described by the Fermat principle in graded-index media. Therefore, the RTE in graded-index media is more difficult to solve analytically except for some limiting cases [11,12].

The commonly used methods for the solution of the radiative transfer budget include (i) the ordinates method (DOM/FVM) [13,14], which defines the angular points to use in the solution procedure; (ii) the stochastic and reverse Monte Carlo method [15,16], which traces the history of each particle from its emission to disappearance; (iii) the spherical harmonics method (SHM), which is a series decomposition of radiative intensity; (iv) the discrete transfer method (DTM) and the ray tracing method (RT), which follows the curvilinear abscissa [17–19]; and (v) the spectral element method (SEM, LSSEM, and meshless method) [20,21]. The ordinate method and the very-low-order of spherical harmonics method are the most popular, and they are generally incorporated in commercial computational software as FLUENT [22–24], COMSOL Multiphysics [25], OpenFoam, and ANSYS [26]. For the case of irregular geometry, applying the radiative inflow boundary condition is a challenge, and several approaches have been developed, including the inaccurate blocked-off procedure [27], which models the complex boundary as a stair step, and the embedded boundary method, which improves the blocked-off method by treating the complex boundary in a Cartesian grid. In addition, the body-fitted coordinates (BFC) and multiblock grid, which matches the complex boundary, have shown a high degree of accuracy in improving the embedded method. Recently, the immersed boundary method, which was initially developed for computational fluid dynamics, was proposed to solve radiative transfer for complex geometries with high accuracy [24,28]. Similar to the blocked-off procedure, the immersed boundary method extends the complex geometry into active and inactive regions separated by a physical boundary. This procedure increases the computational effort and requires additional storage memory.

---

[*]ymeliguillaume@gmail.com

[†]wangcunhai@ustb.edu.cn

In addition to the difficulty of matching the boundary of the complex geometry, the bending of rays in graded-index media [17–19] is another origin of errors that affect the spatial resolution or accuracy of the radiative solution [29]. To mitigate these errors, high-resolution schemes such as the discontinuous finite elements/Galerkin method [20,30], a flux limiter, and the semianalytic method [31] have been recently used for radiative transfer solutions. Moreover, the mesoscopic lattice Boltzmann method (LBM) for computational fluid dynamics [32] has been extended to a large number of engineering applications, such as heat and mass transfer, and acoustic and phonon transport, and it has been proposed as an efficient method for transient radiations. Regarding the angular directions as macroscopic velocities, Wang *et al.* [33] treat the transient RTE as a case of the convection-diffusion equation without the diffusion term, and they provide a complete description of the lattice Boltzmann formulation (LBM) while the Chapman-Enskog expansion was necessary to recover the nondimensional parameters of the problem. This method has recently gained extraordinary popularity in the radiative transfer domain for both steady and transient studies [24,34–37], and some versions have been presented for radiation problems in which the fictitious speed of light is tuned along each direction of the ray [38,39]. Very recently, a complete version of the first attempt of the RTE solution for graded-index media with the LBM was presented by Liu *et al.* [40]. But unfortunately, the proposed formulation fails to recover the macroscopic RTE in multidimensional problems in the Chapman-Enskog analysis, and therefore it should be amended.

To extend the applicability of the LBM method for both graded-index media and irregular geometries, the complex geometry known as the physical domain is mapped with an element set compatible with the shape of the boundary, and the real nonorthogonal grid is converted into a fictitious orthogonal grid called the computational domain. The Jacobean matrix approach is used to perform the grid transformation into a structured orthogonal grid that is straightforward to generate [41], and on which the lattice Boltzmann method works without extra effort.

The paper is organized as follows: the first part presents the mathematical model and the methodology step by step to build the solution. The second part is first devoted to testing the accuracy of the proposed method, and subsequently to investigating the transient radiation in graded-index media with regular or irregular geometries. Afterwards, the effects of various optical parameters on radiometric quantities are tested.

II. PROBLEM STATEMENT

A. Governing equations in graded-index media

The RTE for graded-index media describing the distribution of the radiative intensity $I(\mathbf{r}, \mathbf{\Omega}, t)$ located at position $\mathbf{r}$ at time t in the direction $\Omega(\theta, \phi)$ is given as [11,42]

$$\frac{n}{c_0}\frac{\partial}{\partial t}I(\mathbf{r}, \mathbf{\Omega}, t) + (\kappa_e + \mathbf{\Omega} \cdot \nabla)I(\mathbf{r}, \mathbf{\Omega}, t)$$

$$+ \frac{1}{n\sin\theta}\frac{\partial}{\partial\theta}\{I(\mathbf{r}, \mathbf{\Omega}, t)(\mathbf{\Omega}\cos\theta - \mathbf{k}) \cdot \nabla n\}$$

$$+ \frac{1}{n\sin\theta}\frac{\partial}{\partial\phi}\{(s_1 \cdot \nabla n)I(\mathbf{r}, \mathbf{\Omega}, t)\} = S(\mathbf{r}, \mathbf{\Omega}, t), \quad (1)$$

where n is the refractive index, $\mathbf{r}$ is the position vector of a given point belonging to the ray path, $\mathbf{\Omega} = \mathbf{i}\,\sin\theta\,\cos\phi + \mathbf{j}\,\sin\theta\,\sin\phi + \mathbf{k}\,\cos\theta$ is the direction vector, and $\mathbf{s}_1 = \mathbf{k} \times \frac{\mathbf{\Omega}}{|\mathbf{k}\times\mathbf{\Omega}|} = -\mathbf{i}\,\sin\phi + \mathbf{j}\,\cos\phi$ $\mathbf{i}$, $\mathbf{j}$, and $\mathbf{k}$ denote the unit vector in a coordinate system, respectively. The radiative properties are the absorption κ_a and scattering κ_s coefficients, which are combined in extinction coefficient $\kappa_e = \kappa_a + \kappa_s$ and the single scattering albedo $\omega = \kappa_s/\kappa_e$. The source term $S(\mathbf{r}, \mathbf{\Omega}, t)$ is simply expressed by [16]

$$S(\mathbf{r}, \mathbf{\Omega}, t) = n^2\kappa_a I_b(T_g) + \frac{\kappa_s}{4\pi}\int_{4\pi}\Phi(\Omega' \rightarrow \Omega)I(\mathbf{r}, \Omega', t)d\Omega',$$
$$(2)$$

where T_g is the medium temperature and $\Phi(\Omega' \rightarrow \Omega)$ is the scattering phase function characterizing the redistribution of the energy from the incoming direction $\Omega'(\theta', \phi')$ to the outgoing direction $\Omega(\theta, \phi)$.

The considered problem is defined under the boundary conditions for $\mathbf{\Omega} \cdot \hat{\mathbf{n}}_w < 0$ and $\mathbf{\Omega}_s \cdot \hat{\mathbf{n}}_w < 0$, where $\hat{\mathbf{n}}_w$ is the normal vector pointing out of the surface, and $\mathbf{\Omega}_s = \mathbf{\Omega} - 2(\mathbf{\Omega} \cdot \hat{\mathbf{n}}_w)\hat{\mathbf{n}}_w$ is the corresponding incident direction of specular reflection. The boundary intensity for $\mathbf{\Omega} \cdot \hat{\mathbf{n}}_w < 0$ is

$$I(\mathbf{r}_w, \mathbf{\Omega}, t) = \mathcal{Q}_{\text{ext}} + \rho_w^s I(\mathbf{r}_w, \mathbf{\Omega}_s, t) + n_w^2\varepsilon_w I_{bw}$$

$$+ \frac{\rho_w^d}{\pi}\int_{\mathbf{\Omega}'\cdot\hat{\mathbf{n}}_w>0}|\mathbf{\Omega}' \cdot \hat{\mathbf{n}}_w|I(\mathbf{r}_w, \Omega', t)d\Omega', \quad (3)$$

where I_{bw} is the blackbody intensity at the boundary, and ρ^s and ρ^d are, respectively, the specular and diffuse reflectivities of the boundary having the emissivity ε_w. The external $\mathcal{Q}_{\text{ext}}$ is the driven force incoming at the external side of the boundary with another direction $\mathbf{\Omega}_0$ given by Snell's law. From the solution of the radiative transfer equation, the radiative flux vector $\boldsymbol{q}(\mathbf{r}, t)$ and incident radiation $G(\mathbf{r}, t)$ at any location $M(x, y)$ are easily calculated as

$$\boldsymbol{q}(\mathbf{r}, t) = \int_{4\pi}\mathbf{\Omega}\,I(\mathbf{r}, \mathbf{\Omega}, t)d\Omega, \quad G(\mathbf{r}, t) = \int_{4\pi}I(\mathbf{r}, \mathbf{\Omega}, t)d\Omega.$$
$$(4)$$

The collimated intensity I_c induced by the laser irradiation undergoes attenuation while propagating within the medium [43,44], and it can be solved analytically with the boundary condition $I_c(\mathbf{r}_w, \mathbf{\Omega}, t) = \mathcal{Q}_{\text{ext}}$. The attenuation of collimated intensity I_c within the medium gives rise to the diffuse intensity $I_d(\mathbf{r}, \mathbf{\Omega}, t)$. Thus, the intensity $I(\mathbf{r}, \mathbf{\Omega}, t)$ is composed of collimated and diffuse components: $I(\mathbf{r}, \mathbf{\Omega}, t) = I_c(\mathbf{r}, \mathbf{\Omega}, t) + I_d(\mathbf{r}, \mathbf{\Omega}, t)$.

B. Coordinate transformations and discretization

The dimensionless time is $t^* = c_0 t/l_c$, where l_c is the critical length, and the spatial operator is rewritten using a new coordinates system $x = x(\xi, \eta)$ and $y = y(\xi, \eta)$, where $0 \leqslant \xi \leqslant 1$ and $0 \leqslant \eta \leqslant 1$ to convert the physical irregular geometry into a regular geometry called the computational domain. The nabla operator becomes $\nabla = \mathbf{A}(\xi, \eta)\nabla^*$, where $\nabla^* = \mathbf{i}\,\nabla_\xi + \mathbf{j}\,\nabla_\eta$, and $\mathbf{A}(\xi, \eta)$ is a second-order tensor defined from the Jacobean transformation by

$$\mathbf{A}(\xi, \eta) = \begin{bmatrix} \xi_x & \eta_x \\ \xi_y & \eta_y \end{bmatrix} = \begin{bmatrix} \frac{y_\eta}{J_a} & -\frac{y_\xi}{J_a} \\ -\frac{x_\eta}{J_a} & \frac{x_\xi}{J_a} \end{bmatrix},$$

$$J_a(\xi, \eta) = x_\xi y_\eta - x_\eta y_\xi. \quad (5)$$

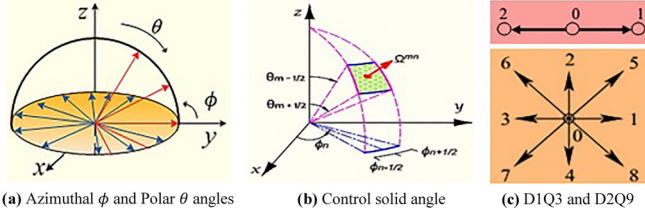**(a)** Azimuthal ϕ and Polar θ angles   **(b)** Control solid angle   **(c)** D1Q3 and D2Q9

FIG. 1. Angular control volumes and spatial lattice arrangement in the LBM for 1D and 2D.

The streaming operator for radiative transfer is expressed as

$$\boldsymbol{\Omega} \cdot \nabla I = \boldsymbol{\Omega} \cdot (\mathbf{A}\nabla^*)I = (\mathbf{A}^T \boldsymbol{\Omega}) \cdot \nabla^* I$$
$$= \nabla^*(\mathbf{A}^T \boldsymbol{\Omega} I) - I\nabla^*(\mathbf{A}^T \boldsymbol{\Omega}), \qquad (6)$$

where $\mathbf{A}^T$ is the transposed matrix of $\mathbf{A}$. The finite-volume method (FVM) [14] is used on a control solid angle as in Fig. 1(b) to cast the angular dependency of the transient RTE in graded-index media for diffuse radiation in the direction $\Omega(\theta^m, \phi^n)$ as

$$n\frac{\partial I_d^{m,n}}{\partial t^*} + l_c \nabla^*\big(\mathbf{A}^T s_*^{m,n} I_d^{m,n}\big) = S_T^{m,n}, \qquad (7)$$

where

$$S_T^{m,n} = l_c \big[S_c^{m,n} + S_d^{m,n} + a_3^{m,n} + a_4^{m,n}$$
$$- \big(\kappa_e + a_1^{m,n} + a_2^{m,n} - \nabla^*(\mathbf{A}^T s_*^{m,n})\big) I_d^{m,n} \big]. \qquad (8)$$

The coefficients are given by

$$a_1^{m,n} = \max\left(\frac{\boldsymbol{\chi}_{m+\frac{1}{2},n}^{\theta}}{\Delta\Omega^{m,n}} \cdot \mathbf{A}\frac{\nabla^* n}{n}, 0 \right)$$
$$+ \max\left(-\frac{\boldsymbol{\chi}_{m-\frac{1}{2},n}^{\theta}}{\Delta\Omega^{m,n}} \cdot \mathbf{A}\frac{\nabla^* n}{n}, 0 \right), \qquad (9a)$$

$$a_2^{m,n} = \max\left(\frac{\boldsymbol{\chi}_{m,n+\frac{1}{2}}^{\phi}}{\Delta\Omega^{m,n}} \cdot \mathbf{A}\frac{\nabla^* n}{n}, 0 \right)$$
$$+ \max\left(-\frac{\boldsymbol{\chi}_{m,n-\frac{1}{2}}^{\phi}}{\Delta\Omega^{m,n}} \cdot \mathbf{A}\frac{\nabla^* n}{n}, 0 \right), \qquad (9b)$$

$$a_3^{m,n} = \max\left(-\frac{\boldsymbol{\chi}_{m+\frac{1}{2},n}^{\theta}}{\Delta\Omega^{m,n}} \cdot \mathbf{A}\frac{\nabla^* n}{n}, 0 \right) I_d^{m+1,n}$$
$$+ \max\left(\frac{\boldsymbol{\chi}_{m-\frac{1}{2},n}^{\theta}}{\Delta\Omega^{m,n}} \cdot \mathbf{A}\frac{\nabla^* n}{n}, 0 \right) I_d^{m-1,n}, \qquad (9c)$$

$$a_4^{m,n} = \max\left(-\frac{\boldsymbol{\chi}_{m,n+\frac{1}{2}}^{\phi}}{\Delta\Omega^{m,n}} \cdot \mathbf{A}\frac{\nabla^* n}{n}, 0 \right) I_d^{m,n+1}$$
$$+ \max\left(\frac{\boldsymbol{\chi}_{m,n-\frac{1}{2}}^{\phi}}{\Delta\Omega^{m,n}} \cdot \mathbf{A}\frac{\nabla^* n}{n}, 0 \right) I_d^{m,n-1}. \qquad (9d)$$

The discrete collimated and diffuse source term $S_d^{m,n}$ is given by

$$S_c^{m,n} = \frac{\kappa_s}{4\pi} \frac{I_c(\mathbf{r}, \boldsymbol{\Omega}_c, t)}{\Delta\Omega^{m,n}} \int_{\Delta\Omega^{m,n}} \Phi(\boldsymbol{\Omega}_c, \Omega) d\Omega, \qquad (10a)$$

$$S_d^{m,n} = n^2 \kappa_a I_b(T_g) + \frac{\kappa_s}{4\pi} \sum_{m'=1}^{N_\theta} \sum_{n'=1}^{N_\phi} \Delta\Omega^{m',n'} I_d^{m',n'} \tilde{\Phi}^{m,n;m',n'}, \qquad (10b)$$

where $\tilde{\Phi}^{m,n;m',n'}$ is the angular mean scattering function for the FVM. The quadrature sets are represented, respectively, by directions and corresponding weights as

$$s_*^{m,n} = \int_{\Delta\Omega^{m,n}} \frac{\boldsymbol{\Omega} d\Omega}{\Delta\Omega^{m,n}}, \quad \Delta\Omega^{m,n} = \int_{\theta^{m-\frac{1}{2}}}^{\theta^{m+\frac{1}{2}}} \int_{\phi^{n-\frac{1}{2}}}^{\phi^{n+\frac{1}{2}}} d\Omega. \quad (11)$$

The recursive formulas for edge direction vectors $\boldsymbol{\chi}_{m\pm\frac{1}{2},n}^{\theta}$ and $\boldsymbol{\chi}_{m,n\pm\frac{1}{2}}^{\phi}$ are

$$\boldsymbol{\chi}_{m+\frac{1}{2},n}^{\theta} - \boldsymbol{\chi}_{m-1/2,n}^{\theta} = \int_{\Delta\Omega^{m,n}} \frac{1}{\sin\theta}\frac{\partial}{\partial\theta}(\boldsymbol{\Omega}\cos\theta - \mathbf{k}) d\Omega, \qquad (12a)$$

$$\boldsymbol{\chi}_{m,n+\frac{1}{2}}^{\phi} - \boldsymbol{\chi}_{m,n-1/2}^{\phi} = \int_{\Delta\Omega^{m,n}} \frac{1}{\sin\theta}\frac{\partial s_1}{\partial\phi} d\Omega, \qquad (12b)$$

where $\boldsymbol{\chi}_{\frac{1}{2},n}^{\theta} = \boldsymbol{\chi}_{N_\theta+\frac{1}{2},n}^{\theta} = 0$ and $\boldsymbol{\chi}_{m,\frac{1}{2}}^{\phi} = \boldsymbol{\chi}_{m,N_\phi+\frac{1}{2}}^{\phi} = \mathbf{j}\Delta\theta^m$. In addition, the solid angle is mapped into $N_\theta \times N_\phi$ directions such that $\theta^m = (m - 0.5)\pi/N_\theta$ and $\phi^n = 2(n - 0.5)\pi/N_\phi$.

C. Lattice Boltzmann method

The consistency of the LBM to recover the macroscopic state of the angular discretized RTE is obtained via the Chapman-Enskog analysis developed in the literature [33–35,40,45]. Here in graded-index media, two possible procedures, known as Procedure 1 and Procedure 2, can be developed to construct the equilibrium distribution functions and source terms. These procedures can be adopted by including the new variable a_0 such that $a_0 = 1$ for Procedure 1 and $a_0 = n(\mathbf{r}^*)$ for Procedure 2. So, in such a situation, Eq. (7) is rewritten as

$$a_0 \frac{\partial I_d^{m,n}}{\partial t^*} + \nabla^*\big[\mathbf{u} I_d^{m,n}(\mathbf{r}^*, \boldsymbol{\Omega}^{mn}, t^*)\big] = F^{m,n}, \qquad (13a)$$

$$F^{m,n}(\mathbf{r}^*, \boldsymbol{\Omega}^{mn}, t^*) = \frac{a_0}{n} S_T^{m,n} + \frac{n}{a_0} I_d^{m,n} \mathbf{u} \cdot \nabla^*\Big(\frac{a_0}{n}\Big), \quad (13b)$$

where $\mathbf{u} = l_c a_0 \mathbf{A}^T s_*^{m,n}/n$ for irregular geometry, and it reduces to $\mathbf{u} = l_c a_0 s_*^{m,n}/n$ for regular geometry. Procedure 1 and Procedure 2 are two possible approaches to construct the equilibrium distribution functions and source term, and these approaches are mathematically taken into consideration by the coefficient a_0. For Procedure 1, Eq. (7) is divided by the refractive index n and $a_0 = 1$, while for Procedure 2, the equilibrium distribution functions are constructed based on Eq. (7) and $a_0 = n(\mathbf{r}^*)$. It should be noted that the two procedures are the same for the RTE in regular and constant

refractive index media. The discretized LBM form associated with Eq. (13a) is given as [33–35,46]

$$\mathrm{f}_k(\mathbf{r}^* + \boldsymbol{e}_k \Delta t^*, t^* + \Delta t^*)$$

$$= \left(1 - \frac{\Delta t^*}{\tau}\right) \mathrm{f}_k(\mathbf{r}^*, t^*)$$

$$+ \frac{\Delta t^*}{\tau} \mathrm{f}_k^{\mathrm{eq}}(\mathbf{r}^*, t^*) + \Delta t^* F_k + \frac{\Delta t^{*2}}{2} \frac{\partial F_k}{\partial t^*}, \qquad (14)$$

where

$$\mathrm{f}_k^{\mathrm{eq}} = w_k I_{\mathrm{d}}^{\mathrm{m,n}}(\mathbf{r}^*, \boldsymbol{\Omega}^{\mathrm{mn}}, t^*)$$

$$\times \left[a_0 + \frac{\boldsymbol{e}_k \cdot \mathbf{u}}{c_s^2} + \frac{(\mathbf{u}\mathbf{u} - c_s^2 a_0^2 \mathbf{I}) : (\boldsymbol{e}_k \boldsymbol{e}_k - c_s^2 \mathbf{I})}{a_0(\alpha_s - 1) c_s^4} \right], \tag{15a}$$

$$F_k = w_k \left[1 + \lambda \frac{\boldsymbol{e}_k \cdot \mathbf{u}}{a_0 c_s^2} \right] F^{\mathrm{m,n}} - \lambda w_k I_{\mathrm{d}}^{\mathrm{m,n}} \frac{\boldsymbol{e}_k \cdot \mathbf{u}}{a_0^2 c_s^2} (\mathbf{u} \cdot \nabla^* a_0)$$

$$+ \lambda_0 w_k \frac{\boldsymbol{e}_k \cdot \mathbf{u}}{a_0 c_s^2} G_0, \tag{15b}$$

with $\mathbf{I}$ representing a unit tensor, c_s is the lattice sound speed, G_0 is a function to be determined, f_k is the k-particle distribution function having the equilibrium state $\mathrm{f}_k^{\mathrm{eq}}$, and w_k is the weight of f_k along the direction vector $\boldsymbol{e}_k$ connecting to the nearest-neighbor node. The lattice isotropy is defined as $\sum_k w_k \boldsymbol{e}_k \boldsymbol{e}_k = c_s^2 \mathbf{I}$ and $\sum_k w_k \boldsymbol{e}_k = \sum_k w_k \boldsymbol{e}_k \boldsymbol{e}_k \boldsymbol{e}_k = 0$.

In the commonly developed LBM in irregular geometries based on BFC in convection analysis, the lattice streaming operator is $\boldsymbol{e}_k \cdot \nabla \mathrm{f}_k = \boldsymbol{e}_k \cdot (\mathbf{A}\nabla^*)\mathrm{f}_k = (\mathbf{A}^T \boldsymbol{e}_k) \cdot \nabla^* \mathrm{f}_k$. So, the lattice vectors $\boldsymbol{e}_k$ are tuned locally at each position into $\mathbf{A}^T \boldsymbol{e}_k$, and $\mathbf{u}$ definitively becomes $\mathbf{u} = l_c a_0 \boldsymbol{s}_*^{\mathrm{m,n}}/n$. In such a case, the known collision-streaming processes of the LBM are no longer applicable, the Runge-Kutta method is used for time integration, and the finite-difference, -volume, or -element methods are used in spatial discretization [47–49]. In this study, Eq. (6) is the primary key for the conservation of the LBM philosophy of collision-streaming with global (constant) streaming vectors $\boldsymbol{e}_k$.

The macroscopic variables are recovered using

$$\sum_k \mathrm{f}_k^{\mathrm{eq}} = a_0 I_{\mathrm{d}}^{\mathrm{m,n}}(\mathbf{r}^*, \boldsymbol{\Omega}^{\mathrm{mn}}, t^*),$$

$$\sum_k \boldsymbol{e}_k \mathrm{f}_k^{\mathrm{eq}} = \mathbf{u} I_{\mathrm{d}}^{\mathrm{m,n}}(\mathbf{r}^*, \boldsymbol{\Omega}^{\mathrm{mn}}, t^*), \tag{16a}$$

$$\sum_k \boldsymbol{e}_k \boldsymbol{e}_k \mathrm{f}_k^{\mathrm{eq}} = \frac{\mathbf{u}\mathbf{u}}{a_0} I_{\mathrm{d}}^{\mathrm{m,n}}(\mathbf{r}^*, \boldsymbol{\Omega}^{\mathrm{mn}}, t^*),$$

$$\sum_k F_k = F^{\mathrm{m,n}}(\mathbf{r}^*, \boldsymbol{\Omega}^{\mathrm{mn}}, t^*), \tag{16b}$$

$$\sum_k \boldsymbol{e}_k F_k = \lambda \mathbf{u} \left(\frac{a_0 F^{\mathrm{m,n}} - (\mathbf{u} \cdot \nabla^* a_0) I_{\mathrm{d}}^{\mathrm{m,n}}(\mathbf{r}^*, \boldsymbol{\Omega}^{\mathrm{mn}}, t^*)}{a_0^2} \right)$$

$$+ \frac{\lambda_0 \mathbf{u}}{a_0} G_0. \tag{16c}$$

The recovering of the RTE for a graded index, and determination of the partial source term G_0, is realized via the

Chapman-Enskog analysis, which expresses G_0 as

$$G_0 = I_{\mathrm{d}}^{\mathrm{m,n}} \left(\frac{\mathbf{u} \cdot \nabla^*(\mathbf{u}\mathbf{u})}{|\mathbf{u}|^2} - \nabla^* \cdot \mathbf{u} \right), \tag{17}$$

where $| |$ is the Euclidian norm. So, the total discrete force F_k is rewritten as

$$F_k = w_k \left(1 + \lambda \frac{\boldsymbol{e}_k \cdot \mathbf{u}}{a_0 c_s^2} \right) F^{\mathrm{m,n}}$$

$$+ \lambda w_k \frac{\boldsymbol{e}_k \cdot \mathbf{u}}{a_0 c_s^2} I_{\mathrm{d}}^{\mathrm{m,n}} \left(\frac{\mathbf{u} \cdot \nabla^*(\mathbf{u}\mathbf{u})}{|\mathbf{u}|^2} - \nabla^* \cdot \mathbf{u} - \frac{\mathbf{u} \cdot \nabla^* a_0}{a_0} \right). \tag{18}$$

The RTE for graded-index media is recovered from the Chapman-Enskog analysis, and different lattice arrangements can also be used in one dimension thanks to the lattice coefficient α_s. In addition, the lattice arrangements for one-dimensional (1D) and two-dimensional (2D) geometries are also represented in Fig. 1, and the corresponding parameters are listed in Table I [50].

Remarks

(i) For the RTE in a rectangular enclosure, $\mathbf{u}$ is a constant vector in Procedure 2 and therefore $G_0 = 0$, justifying that Procedure 2 is simpler to code than Procedure 1.

(ii) In addition, if the refractive index is constant, then $\nabla^* a_0 = 0$, therefore only the first term in brackets is considered in Eq. (18), which indicates that the present LBM can be naturally degenerated to handle the RTE in inhomogeneous media with a constant refractive index.

(iii) In one-dimensional problems, Eq. (B5) in Appendix B shows that Procedure 1, where $a_0 = 1$ and $\nabla^* a_0 = 0$, is equivalent to the formulation recently proposed by Liu *et al.* [40]. However, for multidimensional problems, their formulation fails to accommodate Eq. (18) in Procedure 1. So, the real and general form of the discrete F_k to consider in graded-index media for Procedures 1 or 2 is given by Eq. (18), which corrects the recent formulation proposed by Liu *et al.* [40].

D. Boundary treatments for the LBM in irregular graded-index media

The boundary conditions of the RTE are the inflow boundary types, and for the outflow boundary $\boldsymbol{\Omega}^{\mathrm{m,n}} \cdot \hat{\mathbf{n}}_w > 0$, the Clausius ray invariant is used to express the radiation intensity as

$$I_{\mathrm{d}}(\mathbf{r}_w, \boldsymbol{\Omega}^{\mathrm{m,n}}, t^*) = \left(1 + \left| \frac{\mathbf{r}_w - \mathbf{r}_a}{\mathbf{r}_{\mathrm{n}a} - \mathbf{r}_a} \right| \right) \frac{n_w^2}{n_a^2} I_{\mathrm{d}}(\mathbf{r}_a, \boldsymbol{\Omega}^{\mathrm{m,n}}, t^*)$$

$$- \left| \frac{\mathbf{r}_w - \mathbf{r}_a}{\mathbf{r}_{\mathrm{n}a} - \mathbf{r}_a} \right| \frac{n_w^2}{n_{\mathrm{n}a}^2} I_{\mathrm{d}}(\mathbf{r}_{\mathrm{n}a}, \boldsymbol{\Omega}^{\mathrm{m,n}}, t^*), \quad (19)$$

where $\mathbf{r}_a$ denotes the location of the adjacent node of $\mathbf{r}_w$, and $\mathbf{r}_{\mathrm{n}a}$ denotes the location of the next adjacent node.

The nonequilibrium extrapolation scheme is used to apply the boundary conditions [33–35,45,46,50,51] to obtain the distribution functions at the boundaries. The boundary intensity is used to compute the equilibrium distribution functions at the wall node, and the radiative intensity at the previous time step is used to compute the equilibrium functions at the interior node neighboring the considered wall [36].

TABLE I. Possible lattice arrangements for D1Q3 used in 1D and for D2Q9 used in 2D [50]. Note: The lattice speed $e = \frac{\Delta\xi^*}{\Delta t^*} = \frac{\Delta\eta^*}{\Delta t^*}$.

| | Sound | | Weights | | Linking vectors $e_{k\neq0}$ |
	speed c_s	α_s	w_0	$w_{k\neq0}$	with $e_0 = (0)$ or $e_0 = (0, 0)$
Lattice					
D1Q3a	$e/\sqrt{3}$	3	2/3	$w_{1-2} = 1/6$	$e_{1,2} = (\pm1)e$
D1Q3b	$e/\sqrt{2}$	2	1/2	$w_{1-2} = 1/4$	$e_{1,2} = (\pm1)e$
D1Q3c	$e/\sqrt{6}$	6	5/6	$w_{1-2} = 1/12$	$e_{1,2} = (\pm1)e$
D2Q9	$e/\sqrt{3}$	3	4/9	$w_{1-4} = 1/9$	$e_{1,3} = (\pm1, 0)e,\ e_{2,4} = (0, \pm1)e$
				$w_{5-8} = 1/36$	$e_{5,7} = (\pm1, \pm1)e,\ e_{6,8} = (\mp1, \pm1)e$

III. RESULTS AND DISCUSSION

In this section, the stability and accuracy of the LBM are first examined by considering some cases available in the literature in order to build the ray and grid-independent solutions. Then, the methodology is used to treat the radiation transport in graded-index media under diffuse or collimated irradiation with combined radiative properties. By considering that $\tau = \Delta t^*$, the grid and ray independence verifications show that 200 lattices and $N_\theta = 96$ discrete directions are adopted for 1D studies, while 40×40 lattices and $N_\theta \times N_\phi = 12 \times 48$ discrete directions are used for 2D problems. The stability condition based on the directional propagation speed in a computational lattice is given as $\min(\Delta x_0^*, \Delta y_0^*)/\Delta t^* \geqslant 1$, where Δx_0^* and Δy_0^* are evaluated on a lattice having a minimal surface as

$$\Delta x_0^* = \int_\xi^{\xi+\Delta\xi} \frac{n(\xi, \eta_{\max})d\xi}{\sin\left(\frac{0.5\pi}{N_\theta}\right)\cos\left(\frac{\pi}{N_\phi}\right)},$$

$$\Delta y_0^* = \int_\eta^{\eta+\Delta\eta} \frac{n(\xi_{\max}, \eta)d\eta}{\sin\left(\frac{0.5\pi}{N_\theta}\right)\cos\left(\frac{\pi}{N_\phi}\right)}. \quad (20)$$

This relation shows that the refractive index and grid size affect the stability. In addition, decreasing N_θ or increasing N_ϕ has a significant effect on the stability, and therefore Δt^* should be chosen judiciously. The value of Δt^* throughout this study has been chosen as $\Delta t^* = 0.001$ to build these results using Procedure 2, except in a few cases with indications where Procedure 1 has also been used.

A. One-dimensional RTE in graded-index media

The first considered case is the transient radiation in an infinite and cold isotropic scattering slab with diffuse or Fresnel walls. The optical thickness of the slab is $\kappa_e L = 1.0$, and the single scattering albedo is $\omega = 0.5$ while the left boundary intensity is suddenly raised at diffuse $I(0, t^*) = I_0 H(t^*)$, where $H(t^*)$ is the Heaviside step function and $I_0 = 1$ W m^{-2}. The medium is bounded by black walls, and the refractive index with linear variation given by $n = 1 + 2z/L$ is considered. Figures 2(a) and 2(b) depict the time evolution of the incident radiation $G(z, t^*)$ and radiative heat flux $q(z, t^*)$ with diffuse walls, built with the most popular D1Q3a lattice structure. These figures show good agreement with discontinuous finite-element method (DFEM) solutions [52], which have been confirmed to be accurate. Moreover, a radiation wavefront reaches any location z at time level $t^* = (\frac{z}{L}) + (\frac{z}{L})^2 = 0.4,\ 1.0,\ 2.0,$ and 4.0 corresponding to

$z/L = 0.306,\ 0.618,\ 1.0,$ and 1.562 observed in Fig. 2. So, the LBM can handle the correct propagation speed of radiations within semitransparent graded-index media. Using the same lattice structure, Figs. 2(c) and 2(d) depict the time variation of the incident radiation and heat flux for the Fresnel wall built with Procedure 1 and Procedure 2. These figures show that the two procedures of the LBM are equivalent and produce the same results. It can also be observed that, considering the right boundary with Fresnel reflectivity, the upstream incident beam with $0.333 < \mu = \cos\theta < 1$ reflects back towards the left boundary while the range $0 < \mu < 0.333$ undergoes total reflection. So, the downstream hemisphere of the right boundary is irradiated, as shown in Fig. 3. As a consequence, the reflected beam increases the incident radiation and decreases the radiative heat flux near the right boundary. These observations demonstrate clearly that the present LBM can handle theoretical phenomena as diffuse, specular, or Fresnel boundary types.

The next considered case is the transient radiative problem in a semitransparent graded-index slab, where the optical thickness of the slab is $\kappa_e L = 1.0$, bounded by vacuum on the left and a nonscattering semi-infinite medium with a constant refractive index $n_L > 1$. The isotropic scattering medium with single scattering albedo $\omega = 1.0$ and refractive index $n = 1 + (n_L - 1)z/L$ is illuminated at the left boundary with a laser beam while the right boundary is free from radiation. The laser pulse normal to the boundary is given by

$$I_w(t) = I_0 \exp\left[-\left(\frac{t - 3t_p}{0.5t_p}\right)^2 \ln2\right][H(t) - H(t - 6t_p)], \quad (21)$$

where $\kappa_e c_0 t_p = 0.4$, and the total computational time span $t^* = 12$ is considered. The collimated beam is given analytically by Beer's law as $I_c(z, t) = I_w(t - \int_0^z \frac{n(y)dy}{c_0})\exp(-\kappa_e z)$. The present LBM is used to build the time-resolved reflectance and transmittance for $n_L = 1$ and 3 and compared in Fig. 4 with the values of the DFEM [52]. To show the universality of the LBM even for very uncommon lattice structures, the D1Q3b and D1Q3c in Procedure 2 are used. The LBM results exhibit good agreement with the DFEM results and demonstrate that the D1Q3b and D1Q3c lattices are also very accurate as D1Q3a and therefore they can be used without loss of accuracy.

The accuracy of the LBM is now investigated by considering an isotropic scattering slab with the optical thickness of $\kappa_e L = 1.0$ made of two layers with different refractive indices and separated by the Fresnel-type interface. Each layer with the optical thickness of $\kappa_e L_0 = 0.5$ is bounded by Fresnel-type
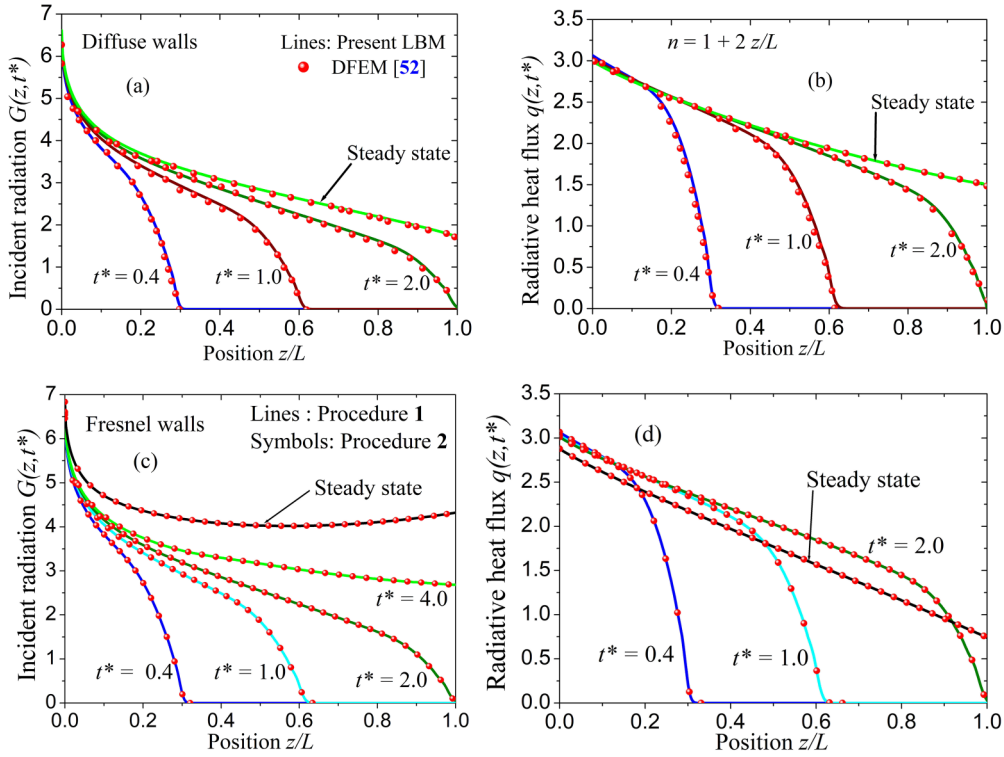
FIG. 2. Incident radiation and radiative heat flux distributions in a cold slab at different time levels for $\omega = 0.5$, $n = 1 + \frac{2z}{L}$, and $\kappa_e L = 1.0$. (a) Incident radiation with diffuse walls. (b) Heat flux with diffuse walls. (c) Incident radiation with Fresnel walls. (d) Heat flux with Fresnel walls.

walls, and the first and second layers have constant refractive indices $n_1 = 1.2$ and $n_2 = 1.5$, respectively. The first layer is irradiated at the left boundary with a single square pulse $I_w(t) = H(t) - H(t - t_p)$ of duration $t_p^* = c_0 t_p/L = 1.0$ with normal incidence and single scattering albedo $\omega = 1.0$, while the right boundary is free from radiation. The collimated remnant of radiation is solved analytically, and it is observed in Fig. 5 that the collimated beam undergoes multiple reflections and transmission, which is due to the refractive index discontinuities at semitransparent boundaries and interfaces. It is also observed that the decreasing collimated intensity shows the discontinuity at the interface, and the analytical solution of the collimated beam agrees very well with the LBM results developed by Zhang *et al.* [38].

Figures 6(a) and 6(b) depict the reflectance and transmittance signals in comparison with the Monte Carlo

method (MCM) developed by Zhang *et al.* [38] for $n_1 = 1.2$ and $n_2 = 1.5$. For this particular case, each layer has been split into 100 lattices and 80 discrete directions to compute the grid and angular independent solutions. It can be realized that an excellent agreement is observed between the present LBM solution and the MCM solutions. Theoretically, the wavefront reaches the right boundary of the second layer at time $c_0 t = n_1 L_1 + n_2(L - L_1) = 1.35$, and the transmittance signal appears and the bond ends at $1.35 + t_p^*$. Due to the laser pulse, the reflectance signal increases during the time period of t_p^*, and the laser switches off. The wavefront undergoes the first reflection at the interface at $c_0 t = n_1 L_1 = 0.6$, giving rise to the first bond in reflectance signal at $c_0 t = 2n_1 L_1 = 1.2$ and the end at $1.2 + t_p^*$, while partial fraction undergoes transmission towards the second layer. Afterwards, this fraction undergoes reflection at the right boundary of the second layer and reaches the left boundary of the first layer at $c_0 t = 2n_1 L_1 + 2n_2(L - L_1) = 2.7$ to start the second bond in reflectance signal which ends at $2.7 + t_p^*$. These theoretical analyses are consistent with the LBM results presented in Fig. 6, which predict the correct propagation speed of radiations.

To investigate the accuracy of the different lattice structures proposed in this LBM model, we consider the case of an infinite slab with a Gaussian-shaped radiative source term $S(z) = n^2 \kappa_a I_b(T_g) = \exp[-\frac{(z/L - c_{00})^2}{\alpha^2}]$ and refractive index $n = 1.0$. The medium is absorbing, emitting, and nonscattering ($\omega = 0$) with black and diffuse surfaces. Both boundaries are subjected to strongly inhomogeneous source terms with a Gaussian intensity $I(z_w, \mu) = S(z_w)/\kappa_e$. The mathematical
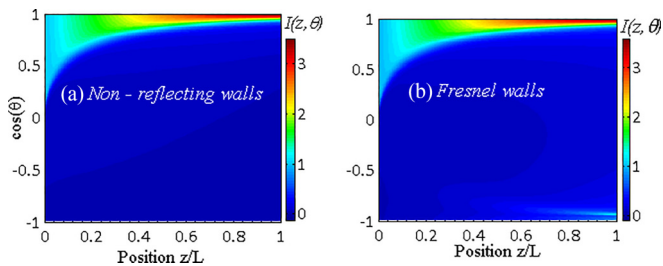

FIG. 3. Angular distribution of radiative intensity $I(z, \theta)$ at steady state for $\omega = 0.5$, $n = 1 + 2z/L$, and $\kappa_e L = 1.0$ with (a) diffuse type walls, (b) Fresnel-type walls.
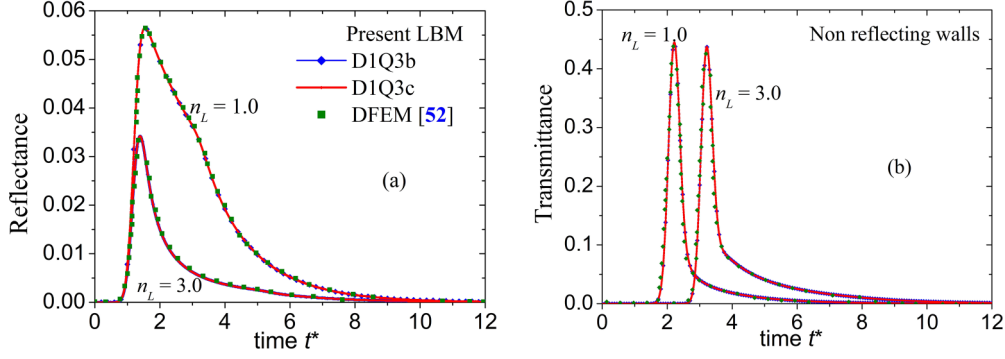
FIG. 4. Time-resolved hemispherical transmittance signals with refractive index $n = 1 + (n_L - 1)z/L$ for $n_L = 1$ and 3.

solution at steady state is defined as [35]

$$I(z^*, \mu) = \frac{1}{\kappa_e} \exp\left(-\frac{\kappa_e z^*}{\mu} - \frac{c_{00}^2}{\alpha^2} \right)$$
$$- \frac{\alpha\sqrt{\pi}}{2\mu} \exp\left\{ -\frac{\kappa_e}{\mu} u_1 \right\} \{u_2(z^*) - u_2(0)\}, \quad (22)$$

where $z^* = \frac{z}{L}$, $\mu > 0$, $u_1 = z^* - (\frac{\alpha^2 \kappa_e}{4\mu} + c_{00})$, and $u_2(z^*) =$ erf$[\frac{\alpha \kappa_e}{4\mu} + \frac{(c_{00}-z^*)}{\alpha}]$. Figure 7 depicts the radiative intensity at $\mu = \cos\theta = 0.113$ and 0.6 for different optical thicknesses $\kappa_e L = 0.1$, 1.0, and 10, and it compares the LBM solution to the exact solution given by Eq. (22). It can be observed that the LBM agrees very well with the analytical solutions.

Moreover, the global relative error given as the summation of $|I_i^{\text{LBM}} - I_i^{\text{exact}}|$ over all nodes i divided by the summation of I_i^{exact} when $c_{00} = 0.5$ and $\alpha = 0.02$ is given in Table II. It has been shown that, for this case the accuracy of the LBM is much higher than that of the other methods, such as the meshless method and the DFEM [35]. This section investigates the accuracy of the different D1Q3a, D1Q3b, and D1Q3c lattice structures for lattice number 20, 50, 100, 150, and 200 to solve the radiative transfer problem defined in the same case. It can be found that for all lattice structures considered, when increasing the grid number, the relative error decreases rapidly. In addition, the accuracy of the D1Q3a is higher than that of D1Q3b, which is also higher than D1Q3c. So, for radiative

transfer problems in 1D, the D1Q3a and D1Q3b are preferable to produce very accurate results than D1Q3c.

B. Two-dimensional RTE in uniform refractive index media

The rectangular enclosure with vertex nodes ABCD in a counterclockwise direction is converted into a square using the transformation $\mathbf{r} = \mathbf{r}_A + (\mathbf{r}_B - \mathbf{r}_A)\xi + (\mathbf{r}_D - \mathbf{r}_A)\eta$, where $\xi = x/L_x$ and $\eta = y/L_y$; $\mathbf{r}_A$, $\mathbf{r}_B$, $\mathbf{r}_C$, and $\mathbf{r}_D$ are the position vectors of the vertex nodes. The steady state is assumed to be achieved with the summation over all nodes i, $\frac{\sum_{i=1}^{\text{all}} |\psi_i^{\text{it}} - \psi_i^{\text{it}-1}|}{\sum_{i=1}^{\text{all}} |\psi_i^{\text{it}-1}|} < 10^{-5}$, where ψ_i^{it} and $\psi_i^{\text{it}-1}$ are the numerical solutions of incident radiation at two consecutive iterations.

The case of an anisotropic scattering square enclosed by black boundaries and square temperatures is $T_g = 1000$ K, $T_{\text{wall}} = 0$ K, and $q_0 = \sigma T_g^4$ is investigated to test the accuracy of the LBM in 2D problems. The considered scattering phase function is given as $\Phi(\mathbf{\Omega}, \mathbf{\Omega}') = 1 + \sum_{i=1}^{8} a_i P_i(\mathbf{\Omega}.\mathbf{\Omega}')$, where P_i is the Legendre polynomial while the a_i coefficients are given by $a_1 = 2.009\,17$, $a_2 = 1.563\,39$, $a_3 = 0.674\,07$, $a_4 = 0.222\,15$, $a_5 = 0.047\,25$, $a_6 = 0.006\,71$, $a_7 = 0.0068$, and $a_8 = 0.000\,050$. In the first consideration, the optical thickness $\kappa_e L = 1.0$, and the effect of three combinations of the single scattering albedos $\omega = 0.0$, 0.5, and 0.9 is investigated. In the second consideration, the scattering albedo is kept at $\omega = 0.0$, and the three optical thicknesses $\kappa_e L = 0.1$, 1.0, and 10 are considered.
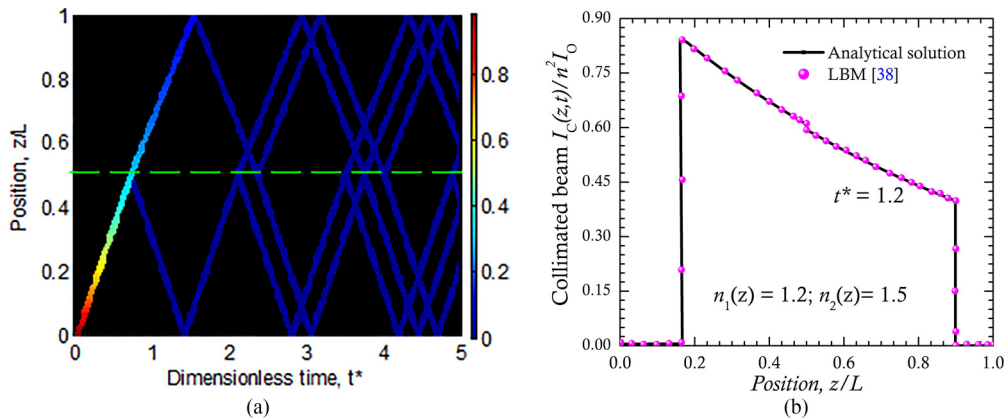

FIG. 5. Behavior of the transient collimated beam for $n_1 = 1.2$ and $n_2 = 1.5$. (a) Multiple reflections and transmissions of the collimated beam when $t_p^* = 0.1$; (b) collimated intensity $I_c(z, t)/(n^2 I_0)$ with normal incidence and $t_p^* = 1.0$ at time level $t^* = 1.2$.
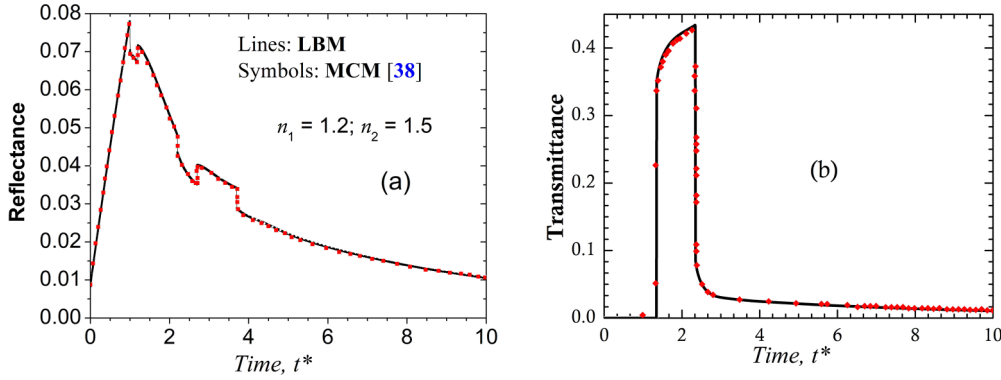
FIG. 6. Time-resolved reflectance and transmittance signals for two-layer slab with Fresnel-type walls and interface with refractive indices $n_1 = 1.2$ and $n_2 = 1.5$.

Figures 8(a) and 8(b) plot the radiative heat flux at the lower wall for the first and second considerations, respectively. It can be found that Fig. 8(a) exhibits good agreement with the least-squares spectral element method (LSSEM) proposed by Zhao and Liu [53], the discrete ordinates method (DOM) [54], and the LBM developed by Yi *et al.* [34] and Liu *et al.* [35], while Fig. 8(b) agrees well with the LBM [34], the finite-element method (FEM), and exact solutions [55].

The case of radiative equilibrium with boundary emission and purely isotropic scattering $\omega = 1.0$ is analyzed in a 2D rectangular enclosure of sizes $L_x \times L_y$ with black walls and temperature distribution $T_L = T_R = T_N = T_g = 0$ K and for $T_S = 1000$ K. In Fig. 9, the discrete transfer method (DTM) solutions proposed by Mishra *et al.* [56] are compared to the LBM solutions for different values of the aspect ratio $L_x/L_y = 0.1$, 1.0, 2.0, and 5.0. It can be observed that the LBM provides accurate results, which agree well with the DTM solutions. So, the LBM accommodates both squared and rectangular geometries in radiative transfer analysis with good accuracy.

Now, the transient collimated radiation is observed in a 2D scattering square of size L and optical thickness $\kappa_e L = 10$ and single scattering albedo $\omega = 0.998$. The left boundary of the cold square is irradiated with a single square pulse $I_w(0, y, t) = H(t) - H(t - t_p)$ of duration t_p such that $\kappa_e t_p^* = \kappa_e c_0 t_p / L = 1.0$ with normal incidence. The scattering phase

function is given as $\Phi(\boldsymbol{\Omega}, \boldsymbol{\Omega}') = 1 + a_1 \, \boldsymbol{\Omega} \cdot \boldsymbol{\Omega}'$, where three values of a_1 for backward scattering ($a_1 = -1$), for isotropic scattering ($a_1 = 0$), and for forward scattering ($a_1 = +1$) are considered. Figure 10 presents the time-resolved transmittance and reflectance signals at locations $\mathcal{A}(0, \, 0.5L)$ and $\mathcal{B}(L, \, 0.5L)$, respectively, and it compares to the least-squares natural element method (LSNEM) solutions from Zhang *et al.* [44]. It is observed that the LBM provides accurate results that agree with benchmark solutions available in the literature.

C. Steady RTE in rectangular media with a graded-index function

The first considered case concerns the radiative problem in an emitting squared enclosure with linear scattering $\Phi = 1 + \boldsymbol{\Omega} \cdot \boldsymbol{\Omega}'$, and refractive index $n = 5[1 - 0.9025x^2/L^2]^{0.5}$ in the first consideration and $n = 5[1 - 0.4356(x^2 + y^2)/L^2]^{0.5}$ in the second [16]. The square temperature is $T_g = 1000$ K, while $T_{wall} = 0$ K and $q_0 = \sigma T_g^4$ with black walls and three combinations of optical properties. Figure 11 presents the radiative heat flux along the lower wall of the enclosure with possible optical thicknesses, boundary emission, and scattering albedos. Comparisons are made between the LBM results and the MCM solution [57] and the DFEM [58] with good accuracy. It can be observed that, as the refractive index decreases, the steady-state heat flux distribution along the line
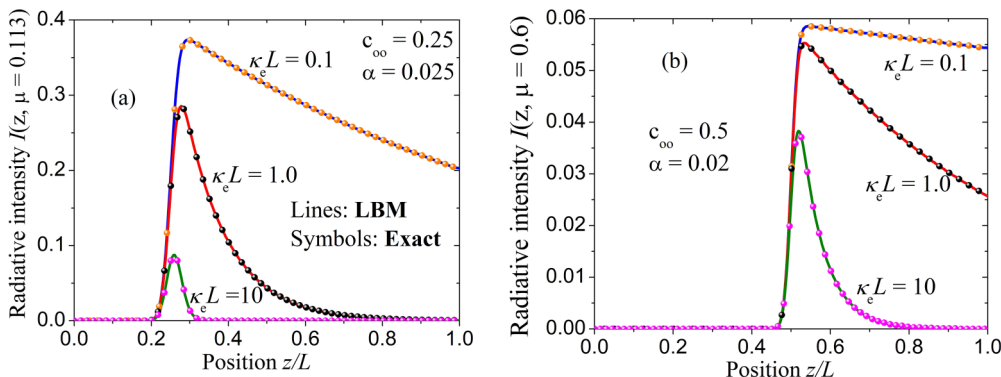

FIG. 7. Radiative intensity for different optical thicknesses $\kappa_e L = 0.1$, 1.0, and 10. (a) For $c_{00} = 0.25$ and $\alpha = 0.025$, and (b) for $c_{00} = 0.5$ and $\alpha = 0.02$.

TABLE II. Global relative error of D1Q3 lattice structures for $c_{00} = 0.5$ and $\alpha = 0.02$.

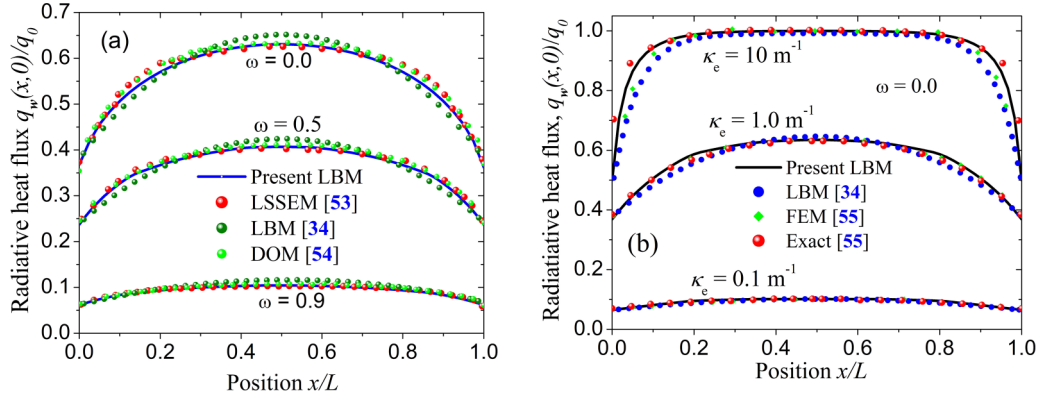| Lattice number	$\kappa_e L = 1.0$			$\kappa_e L = 10$		
	D1Q3a	D1Q3b	D1Q3c	D1Q3a	D1Q3b	D1Q3c
20	1.431(−2)[a]	1.660(−2)	2.860(−2)	6.410(−2)	7.448(−2)	1.200(−1)
50	1.479(−4)	1.501(−3)	1.601(−3)	8.118(−4)	8.501(−3)	9.201(−3)
100	2.391(−5)	3.621(−4)	3.646(−4)	1.349(−4)	2.101(−3)	2.200(−3)
150	1.024(−5)	1.599(−4)	1.607(−4)	5.783(−5)	9.423(−4)	9.542(−4)
200	5.671(−6)	8.972(−5)	9.016(−5)	3.215(−5)	5.309(−4)	5.316(−4)

[a]Read as 1.431×10^{-2}.

FIG. 8. Radiative heat flux at the lower wall for different optical properties at $T_g = 1000$ K and $T_{wall} = 0$ K (a) for $\kappa_e L = 1.0$ and $\omega = 0.0$, 0.5, and 0.9; (b) for $\omega = 0.0$ and $\kappa_e L = 0.1$, 1.0, and 10.
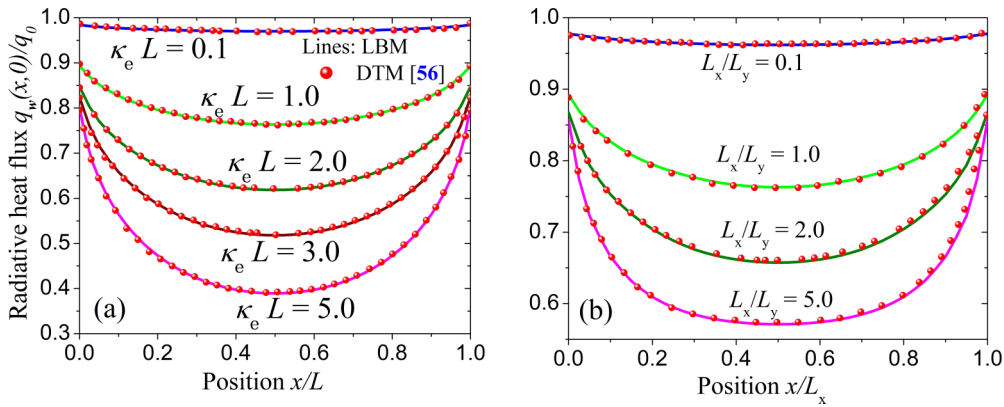

FIG. 9. Radiative heat flux at the bottom wall when $\omega = 1.0$ (a) for $L_x = L_y = L$ with optical thickness $\kappa_e L = 0.1$, 1.0, 2.0, 3.0, and 5.0, and (b) for $L_x/L_y = 0.1$, 1.0, 2.0, and 5.0 with $\kappa_e = 1\,\mathrm{m}^{-1}$.
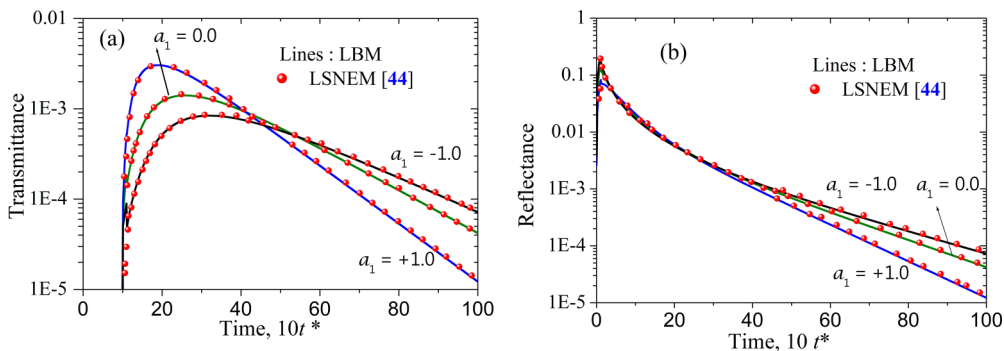

FIG. 10. Time-resolved reflectance and transmittance for three linear scattering laws in a square enclosure. (a) Transmittance signal, (b) reflectance signal.
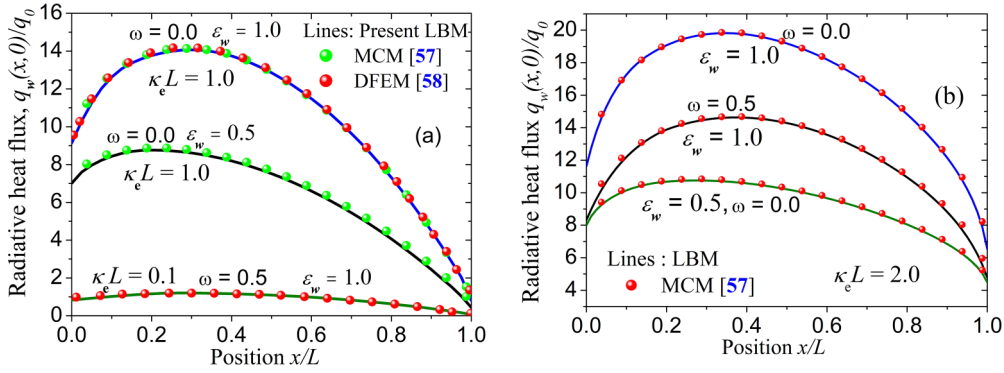
FIG. 11. Radiative heat flux along the lower wall $y = 0$ of the square with $q_0 = \sigma T_g^4$ for (a) $n = 5[1-0.9025x^2/L^2]^{0.5}$ and (b) optical thickness $\kappa_e L = 2.0$ and refractive index $n = 5[1-0.4356(x^2+y^2)/L^2]^{0.5}$.

$y = 0$ presents a local maximum with amplitude depending on the optical properties. The location of this maximum along the x-axis is near the location of the maximum refractive index and does not strongly depend on the optical properties. This is due to the fact that, since the enhancing factor of radiation is proportional to $n^2 I_b(T_g)$, which vanishes at the cold boundaries, local extrema can be necessarily found in the continuous heat flux distribution in the hot medium.

Using the same scattering law, $\Phi = 1 + \mathbf{\Omega} \cdot \mathbf{\Omega}'$ and the temperatures of the south, right, and north boundaries are $T_S = T_R = T_N = 0$ K while the left boundary has $T_L = 1000$ K and $q_0 = \sigma T_L^4$; the radiative heat flux at the lower boundary $(y = 0)$ is presented in Fig. 12. In Fig. 12(a), the optical thickness $\kappa_e L = 2.0$ and refractive index $n = 5[1-0.4356(x^2+y^2)/L^2]^{0.5}$ are used while $\kappa_e L = 1.0$ and $n = 5[1-0.9025x^2/L^2]^{0.5}$ are used to build Fig. 12(b) for three combinations of optical properties. Figure 12 shows excellent agreement between the LBM results and the benchmark solutions produced by the MCM [57] and the FVM [57]. It can also be found that, due to the forward nature of the scattering function, the case with nonzeros scattering albedo dominates the nonscattering radiations cases with zero scattering albedo. The dimensionless heat flux along the line $y = 0$ achieves a certain extremely high value at position $x = 0$ due to the combination of two aspects: the maximum temperature and the refractive to index at the same location $(x = 0)$.

The next case concerns the square of size L with optical thickness $\kappa_e L = 0.1$ and single scattering albedo $\omega = 1.0$ (isotropic scattering). The temperatures of the left, right, and north boundaries are $T_L = T_R = T_N = 0$ K, and the south boundary has $T_S = 1000$ K and $q_0 = \sigma T_S^4$ while the refractive index is set as $n = 1 + 2(x + y)/L$. By considering the same refractive index and optical thickness, the second test case concerns the square with forward scattering law $\Phi = 1 + \mathbf{\Omega} \cdot \mathbf{\Omega}'$ bounded by black walls and temperatures kept at $T_g = 1000$ K, $T_{wall} = 0$ K, and $q_0 = \sigma T_g^4$. Using Procedures 1 and 2 of the LBM scheme, Figs. 13(a) and 13(b) present the radiative heat flux at the lower boundary for three possible wall emissivities $\varepsilon_w = 0.1, 0.5,$ and 1.0 associated with $\omega = 1.0$ in the first test problem and for three scattering albedos $\omega = 0.0, 0.5$ and 0.9 in the second consideration. It can be found that both Procedures 1 and 2 of the LBM exhibit good agreement with the finite-element method (FEM) [59], the FVM and the LSSEM [60]. It can also be observed that the two procedures of the LBM are very accurate and equivalent. Moreover, the spatial distribution of the heat flux increases with position vector as well as the refractive index. In Fig. 13(a), the maximum heat flux along the hot wall $(y = 0)$ is obtained at the location with the maximum refractive index $(y = L)$. Meanwhile, in Fig. 13(b) the heat flux distribution along the cold wall $(y = 0)$ shows a local maximum near the location of the maximum refractive index $(y = L)$. This last observation is due to the fact that, since the enhancing factor of radiation is proportional to

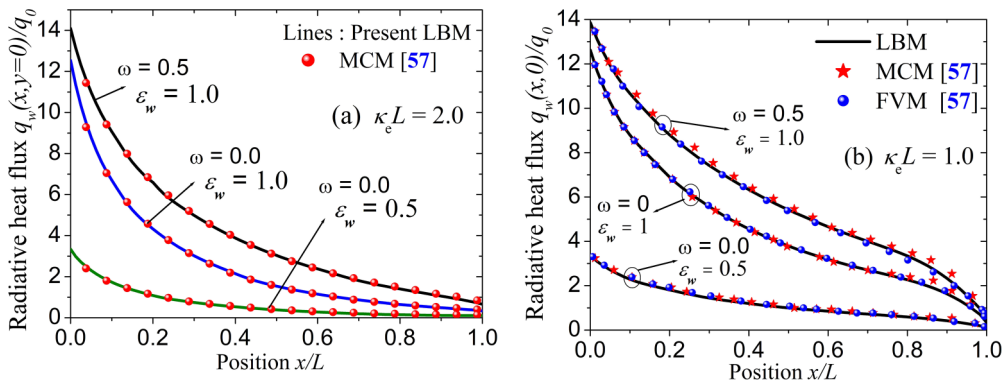

FIG. 12. Radiative heat flux along the wall $y = 0$ of the square with $q_0 = \sigma T_L^4$ for (a) $\kappa_e L = 2.0$ and $n = 5[1-0.4356(x^2+y^2)/L^2]^{0.5}$, (b) $\kappa_e L = 1.0$ and $n = 5[1-0.9025x^2/L^2]^{0.5}$.
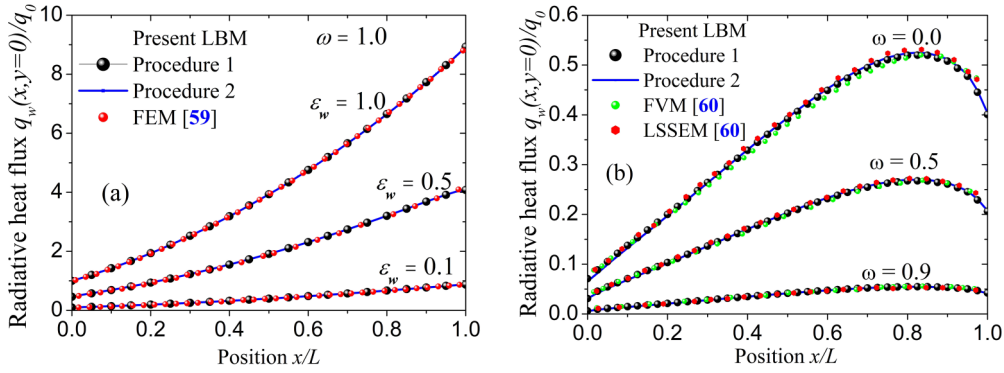
FIG. 13. Radiative heat flux at the lower wall of the square for $n = 1 + 2(x + y)/L$ and $\kappa_e L = 0.1$. (a) Isotropic scattering, $\omega = 1.0$ and $q_0 = \sigma T_S^4$; (b) linear scattering, $\epsilon_w = 1.0$ and $q_0 = \sigma T_g^4$.

$n^2 I_b(T_g)$, which vanishes at the cold boundaries, as was stated previously in Fig. 11, local extrema can be necessarily found in the continuous heat flux distribution in the hot medium.

Consider the case of a nonscattering ($\omega = 0.0$) medium with optical thickness $\kappa_e L = 1.0$ bounded by black walls. The first test case concerns the square enclosure at radiative equilibrium when the temperatures of the left, right, and north boundaries are $T_L = T_R = T_N = 0$ K while the south boundary has $T_S = 1000$ K. Figure 14 shows the radiative equilibrium temperature distributions $T(x, y)/T_S$ at $x/L = 0.325$ for two boundary emissivities $\varepsilon_w = 0.5$, 1.0, and the radial refractive index $n = 5[1 - 0.4356(x^2 + y^2)/L^2]^{0.5}$. For this particular case, the angular discretization $N_\theta \times N_\phi = 12 \times 72$ has been used to obtain the case with a boundary emissivity of 0.5. Figure 14 shows excellent agreement with the benchmark solutions produced by the MCM [57]. In addition, since the maximum refractive index is achieved at the hot boundary, the factor $n_w^2 \varepsilon_w I_{bw}$ enhances the radiative transfer particularly at the hot boundary, and consequently the decreasing absolute value of the temperature rate from hot to cold wall and temperature slip at the boundary walls can be observed. Also, the absolute value of the temperature rate decreases with the emissivity power ε_w due to the fact that the enhancing factor is proportional to ε_w.

The second case is a hot medium bounded by cold walls ($T_{\text{wall}} = 0$ K). Figures 15 and 16 show the incident radiation contours at steady state and four refractive index distributions used when the boundaries are diffused or Fresnel reflecting types. It can be observed in Fig. 15 that the maximum incident radiation is achieved at the boundary point having the maximum refractive index for a Fresnel reflection boundary type, and for a diffuse boundary type this maximum is located near the boundary point having the maximum refractive index. It can be found that incident radiations at steady state presented for the Fresnel boundary walls are slightly more important than the case of diffuse nonreflective walls. This is mainly due to the fact that each radiation beam emanating from the medium with diffuse and nonreflective walls is directly transferred to the environment after hitting the boundaries. So, the reflectivity coefficient due to the refractive index discontinuity at the boundaries induces increasing incident energy since the same ray undergoes many reflections in 2D before being absorbed completely. In the case describes in Fig. 16, the refractive index $n = 1.5 + 0.4 \sin(\frac{\pi x}{L}) + 0.2 \cos(\frac{4\pi y}{L})$ presents local extrema in the spatial domain, and it shows one period along the x-axis and two periods along the y-axis as plotted by Zhang *et al.* [42]. It can be found once more that the LBM is an efficient method that can also handle the radiative transfer when the refractive index presents local extrema in the spatial variation.

D. Two-dimensional RTE in irregular geometries

The popular finite-element method and variants [20,30,53,55,58] are always recognized as powerful tools to capture the macroscopic variables in irregular geometries with or without structured grids. But the computational time increases rapidly for grid refinement. Besides this formulation, the blocked-off and immersed boundary methods [24,27,28] have been proposed for simulations in irregular geometries, whereas the computational effort and storage memory are increased due to the spatial inactive zone. In this section, the transfinite interpolant is used to generate the body-fitted coordinates [61], and Eq. (5) is evaluated analytically. Using $l_c = 1$ m for irregular geometries, the
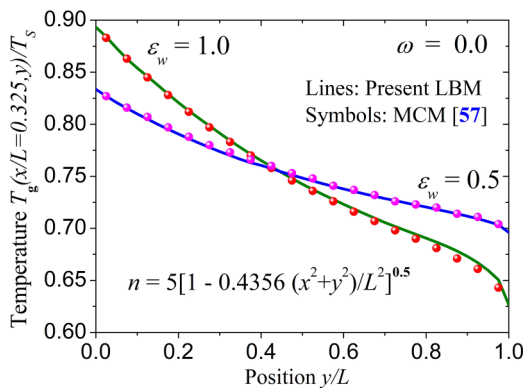

FIG. 14. Temperature distributions for two-dimensional radiative equilibrium with refractive index $n = 5[1 - 0.4356(x^2 + y^2)/L^2]^{0.5}$ and optical thickness $\kappa_e L = 1.0$.
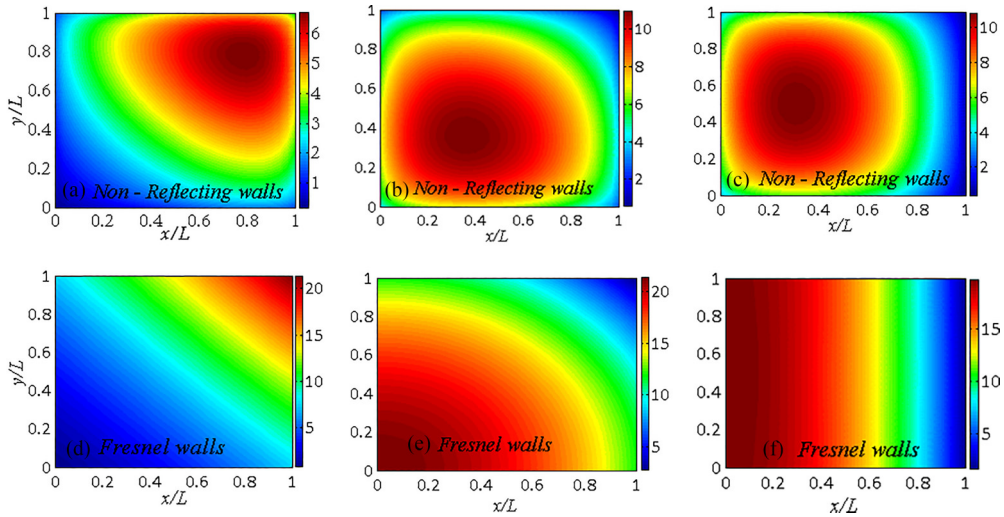
FIG. 15. Incident radiation $G(x, y)/4q_0$ at steady state with $\omega = 0.0$ for diffuse nonreflecting and Fresnel walls for (a) and (d) $n = 1 + 2(x + y)/L$, (b) and (e) $n = 5[1 - 0.4356(x^2 + y^2)/L^2]^{0.5}$, (c) and (f) $n = 5[1 - 0.9025x^2/L^2]^{0.5}$.
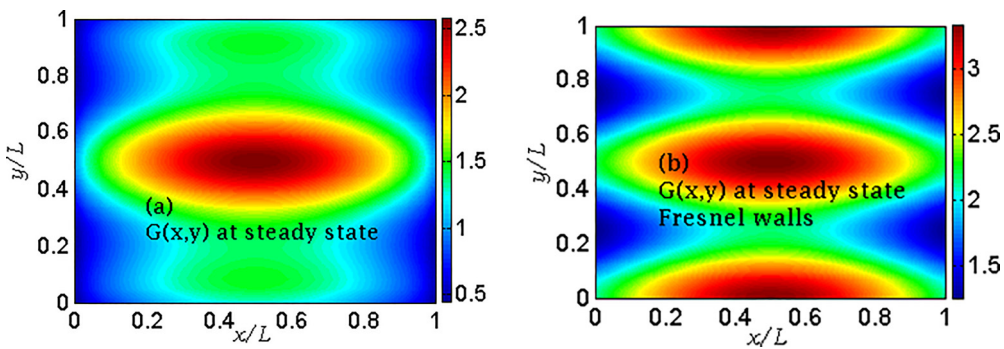
FIG. 16. Incident radiation $G(x, y)/4q_0$ at steady state with $\omega = 0.0$ for sinusoidal refractive index $n = 1.5 + 0.4 \sin(\pi x/L) + 0.2 \cos(4\pi y/L)$ having local extrema located at the center of the square for (a) diffuse nonreflecting walls and (b) Fresnel walls.

FIG. 17. Radiative heat flux at the bottom wall of Geometry **1** and **2** when $\omega = 0.0$ for three extinction coefficients $\kappa_e = 0.1$, 1.0, and 10 m^{-1}.

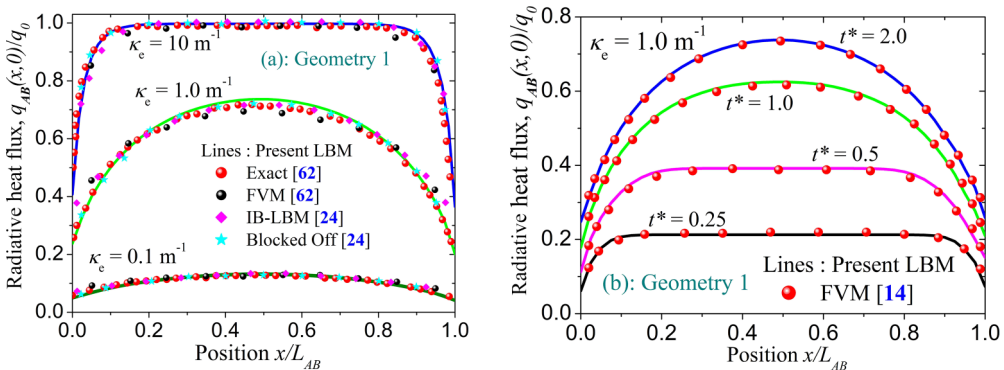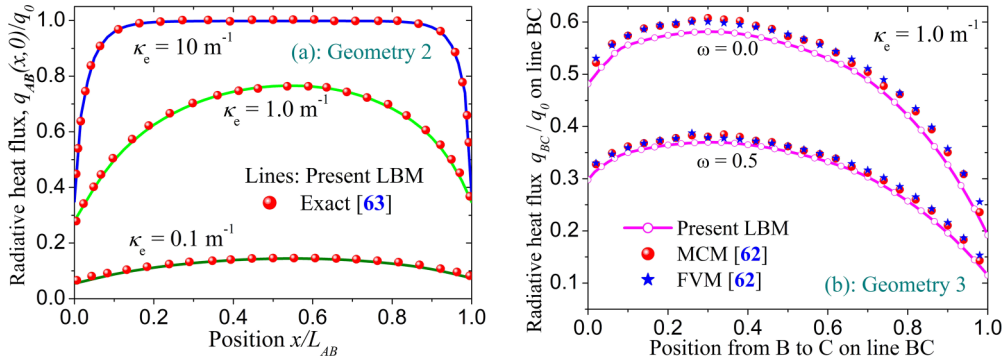FIG. 18. Radiative heat flux at the boundaries. (a) Bottom wall (line AB) of Geometry 2, and (b) right wall (line BC) of the rhombic Geometry 3.

cases of constant refractive indices are validated before introducing the graded-index function to diversify the validity of this proposed LBM.

1. Irregular geometries with constant refractive indices

First, let us consider the test case of the RTE involving an irregular quadrilateral enclosure with vertex nodes ABCD, which is converted into a square of size 1 by the BFC using the transformation $\mathbf{r} = \mathbf{r}_A + (\mathbf{r}_B - \mathbf{r}_A)\xi + (\mathbf{r}_D - \mathbf{r}_A)\eta + (\mathbf{r}_C - \mathbf{r}_B + \mathbf{r}_A - \mathbf{r}_D)\xi\eta$. The emitting-absorbing hot medium with temperature $T_g = 1000$ K, $T_{\mathrm{wall}} = 0$ K, and $q_0 = \sigma T_g^4$ is bounded by black walls and the scattering albedo $\omega = 0.0$. The quadrilateral geometry commonly investigated in the literature with vertex nodes A(0, 0), B(2.2, 0), C(1.5, 1.2), and D (0.5, 1.0) is namely Geometry 1 [62]. The radiative heat fluxes on the bottom wall of Geometry 1 at steady state are shown in Fig. 17(a) for extinction coefficients $\kappa_e = 0.1$, 1.0, and 10 m^{-1}, and comparisons are made with benchmark solutions built with exact solution methods [62], the FVM [62], and the immersed boundary LBM (IB-LBM) [24]. In Fig. 17(b), the transient state of the bottom heat flux of Geometry 1 at time levels $t^* = c_0 t/l_c = 0.25$, 0.5, 1.0, and 2.0 is recorded for $\kappa_e = 1.0$ m^{-1} and compared to the FVM solutions built by Chai [14]. These figures show excellent agreement between the present LBM formulation and benchmark solutions.

Secondly, two quadrilateral enclosures—where the first has vertex nodes A(0, 0), B(2, 0), C(1.5, 2), and D(0.5, 1.0), namely Geometry 2 [63] (all dimensions in meter), and the second is a rhombic quadrilateral enclosure with vertex nodes A(0, 0), B(1, 0), C(1.5, $\frac{\sqrt{3}}{2}$), and D(0.5, $\frac{\sqrt{3}}{2}$) (dimensions in meter), namely Geometry 3—are considered. For the two irregular geometries, the medium is hot and bounded by cold and black walls. The radiative heat flux on the bottom wall (line AB) of the nonscattering Geometry 2 at steady state is shown in Fig. 18(a) for extinction coefficients $\kappa_e = 0.1$, 1.0, and 10 m^{-1}, and comparisons are made with exact solutions [63]. In addition, using the extinction coefficient $\kappa_e = 1.0$ m^{-1}, the participating medium scatters isotropically. Then Fig. 18(b) presents the steady radiative heat flux at the right wall (line BC) of Geometry 3 for two scattering albedos with comparisons with the FVM and the MCM [62]. It can be observed that, for Geometry 2, the LBM solutions agree very well with the exact solutions, while a slight difference can be observed between the present method and the MCM and the FVM in the case of Geometry 3, and the LBM underestimates the radiative heat flux. This can be attributed to the false scattering phenomenon in multidimensional radiative transfer analysis.

Afterwards, setting the extinction coefficient to $\kappa_e = 2.0$ m^{-1} and $\omega = 0.5$, the bottom wall of the isotropic scattering medium is hot while the media and other walls are cold and black. Figure 19 plots the contours of the incident radia-
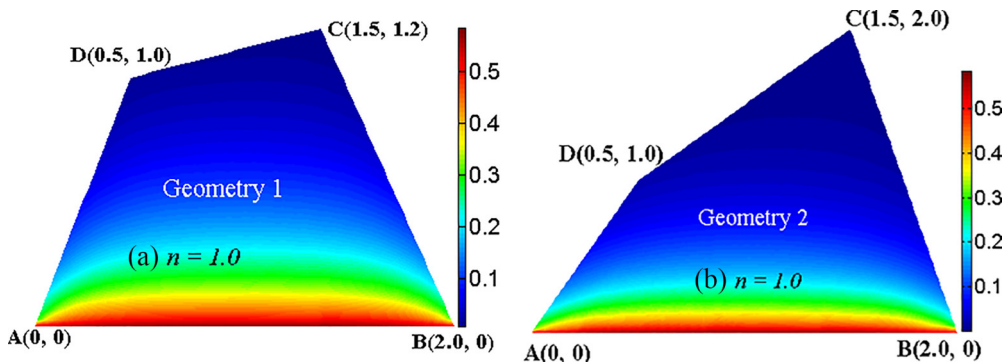

FIG. 19. Contours of the incident radiation $G(x, y)/4q_0$ for $\omega = 0.5$ in Geometries **1** and **2** when $\kappa_e = 2.0$ m^{-1}, $n = 1.0$, and the bottom wall is hot.
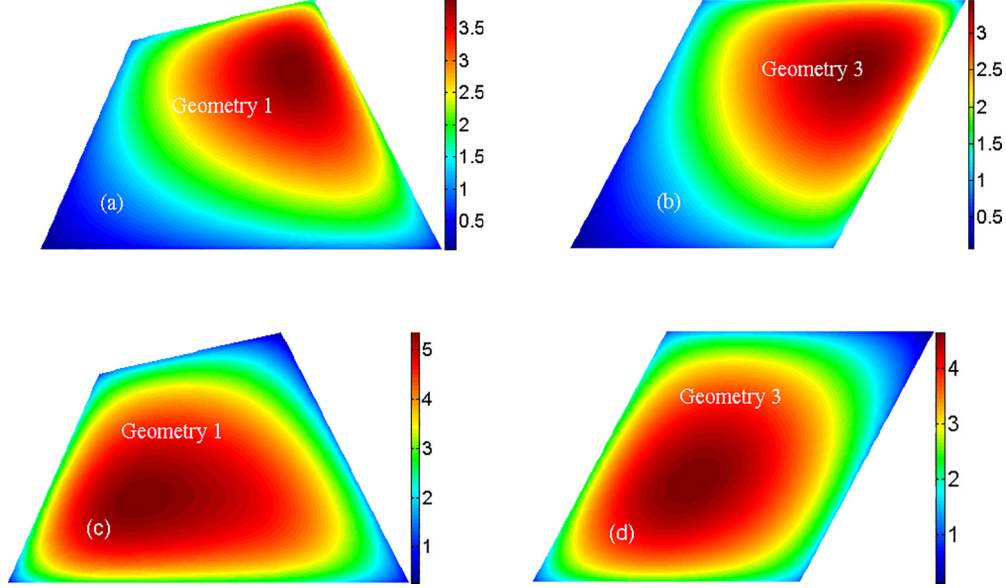
FIG. 20. Contours of the incident radiation $G(x, y)/4q_0$ for irregular Geometries **1** and **3** with graded-index functions (a) and (b) $n = 1 + 2(\xi + \eta)$, and (c) and (d) $n = 5[1-0.4356(\xi^2 + \eta^2)]^{0.5}$.

tion at steady state for the two geometries when considering diffuse walls with $n = 1.0$.

2. Irregular geometries with graded-index distribution

The last results presented concern the nonscattering radiative transfer in a hot ($q_0 = \sigma T_g^4$) irregular geometry with a graded-index function bounded by black, diffuse, and cold walls. It can be observed in Fig. 20 that the hot spot that appears in the solution of the incident radiation adapts the geometry shape near the corner having the maximum refractive index. It can also be found that the incident radiation for a decreasing refractive index $n = 5[1-0.4356(\xi^2 + \eta^2)]^{0.5}$ is relatively higher than the case with increasing refractive index $n = 1 + 2(\xi + \eta)$. This can be attributed to the fact that the source term of the RTE is proportional to $n^2\sigma T_g^4$, and the case with $n = 5[1-0.4356(\xi^2 + \eta^2)]^{0.5}$ has the higher refractive index difference $\Delta n = n_{max} - n_{min}$ for the same $n_{max} = 5$.

Following the methodology described in this work, a MATLAB code is built on a personnal genuine Intel (R) Core™ i5–3230M processor with 2.6 GHz central processing unit (CPU) and 8 GB RAM. The computational cost, which represents the executive time per time step during numerical

simulation, is investigated in this section. The nonscattering radiations are considered in a hot medium with irregular Geometry 1 bounded by black, cold, and Fresnel boudary type. The considered refractive index is a sinusoidal function $n = 1.5 + 0.4\sin(\pi\xi) + 0.2\cos(4\pi\eta)$, which presents local extrema in the spatial domain, and the extinction coefficient is $\kappa_e = 1.0 \text{ m}^{-1}$. Using a dimensionless time step $\Delta t^* = 0.001$, the CPU time of the first time iteration and the total CPU time to reach the steady state are presented in Table III. It can be observed that either grid or angular refinement increases the computational time considerably. Also, the computational time increases more rapidly when the angular mesh is refined rather than the grid refinement, and the combination of the two refinements leads to accurate results within a reasonable computation time.

IV. CONCLUSION

This work establishes the 1D and 2D formulation of the LBM to simulate the RTE in irregular geometries with a graded-index function. Based on the Chapman-Enskog analysis, two possible approaches are proposed to construct the equilibrium distribution functions and source term using the

TABLE III. CPU time for the first time iteration and CPU time to obtain the 2D steady-state distribution of the diffuse incident radiation with LBM and time step $\Delta t^* = 0.001$.

	$N_\theta \times N_\phi = 8 \times 12$		$N_\theta \times N_\phi = 12 \times 48$	
Mesh $N_x \times N_y$	First time step (ms)	Steady state (s)	First time step (s)	Steady state (s)
21×21	18	11 min 53 s	1.8	01 h 50 min 32 s
31×31	26	18 min 14 s	3.1	02 h 49 min 40 s
41×41	38	33 min 11 s	5.0	**05 h 09 min 07 s**
61×61	57	1 h 5 min 22 s	9.2	10 h 08 min 57 s

local radiative direction. In addition, the construction of equilibrium distribution functions accounts for the use of several lattice structures to diversify the framework of the LBM. First, the LBM with three lattice arrangements of D1Q3 is applied for the RTE in 1D problems with a graded-index function involving one or two layers subjected to diffuse or collimated radiations. Afterwards, the RTE in 2D graded-index media with regular geometries under diffuse or collimated radiations is investigated with the D2Q9 scheme. Then, the LBM is extended in 2D irregular geometries with/without a graded index. Numerical experimentations show that the LBM is an efficient, robust, stable, and accurate solution method for transient or steady states of the RTE in complex geometries with a graded index, and therefore it is strongly recommended. Due to the limits of the present work, it would be quite difficult to adapt the methodology to situations with point source heating as a hot spot and with time variation of optical properties, and also for irregular geometries where the Jacobean transformation matrix **A** and its partial derivatives present some singularity points in the computational domain.

We plan to perform in future works the RTE in 3D irregular geometry with the LBM proposed in this paper to build reference data for some of the challenges mentioned by Howell and Mengüç [64].

APPENDIX A: THE CHAPMAN-ENSKOG ANALYSIS

The main idea of this process consists in expanding the time, distribution function, and space with a small expansion parameter ε known as the Knudsen number: $t^* = \varepsilon^{-1}t_1 + \varepsilon^{-2}t_2$, $\mathrm{f}_k = \mathrm{f}_k^{\mathrm{eq}} + \varepsilon \mathrm{f}_k^{(1)} + \varepsilon^2 \mathrm{f}_k^{(2)}$, $F_k = \varepsilon F_k^{(1)} + \varepsilon^2 F_k^{(2)}$, $\partial_{t^*} = \varepsilon \partial_{t_1} + \varepsilon^2 \partial_{t_2}$, $F^{\mathrm{m,n}} = \varepsilon F^{(1)} + \varepsilon^2 F^{(2)}$, $G_0 = \varepsilon G_0^{(1)}$, and $\nabla^* = \varepsilon \nabla_1$. The following constraints are imposed:

$$\sum_k \mathrm{f}_k^{(j)} = 0, \quad \sum_k F_k^{(j)} = F^{(j)} \quad (j > 0), \tag{A1}$$

$$\sum_k \boldsymbol{e}_k F_k^{(1)} = \lambda \mathbf{u} \left(\frac{a_0 F^{(1)} - I_{\mathrm{d}}^{\mathrm{m,n}}(\mathbf{u} \cdot \nabla_1 a_0)}{a_0^2} \right) + \lambda_0 G_0^{(1)} \frac{\mathbf{u}}{a_0}, \tag{A2}$$

$$\sum_k \boldsymbol{e}_k F_k^{(2)} = \frac{\lambda \mathbf{u}}{a_0} F^{(2)}. \tag{A3}$$

The time and spatial Taylor expansion of the term $\mathrm{f}_k(\mathbf{r^*} + \boldsymbol{e}_k \Delta t^*, t^* + \Delta t^*)$ is given by

$$\mathrm{f}_k(\mathbf{r^*} + \boldsymbol{e}_k \Delta t^*, t^* + \Delta t^*) = \mathrm{f}_k(\mathbf{r^*}, t^*) + \Delta t^* D_k \mathrm{f}_k + \frac{\Delta t^{*2}}{2} D_k^2 \mathrm{f}_k + O(\Delta t^{*3}), \tag{A4}$$

where $D_k = \partial_{t^*} + \boldsymbol{e}_k \nabla^*$. Setting $D_{1k} = \partial_{t_1} + \boldsymbol{e}_k \nabla_1$, Eq. (14) is separated at order ε and ε^2 as

$$\varepsilon \ : \ \partial_{t_1} \mathrm{f}_k^{\mathrm{eq}} + \boldsymbol{e}_k \nabla_1 \mathrm{f}_k^{\mathrm{eq}} = F_k^{(1)} - \frac{\mathrm{f}_k^{(1)}}{\tau}, \tag{A5}$$

$$\varepsilon^2 \ : \ \partial_{t_2} \mathrm{f}_k^{\mathrm{eq}} + \left(1 - \frac{\Delta t^*}{2\tau} \right) D_{1k} \mathrm{f}_k^{(1)} + \frac{\Delta t^*}{2} \boldsymbol{e}_k \nabla_1 F_k^{(1)} = F_k^{(2)} - \frac{\mathrm{f}_k^{(2)}}{\tau}, \tag{A6}$$

$$\boldsymbol{e}_k \mathrm{f}_k^{(1)} = -\tau \big[\partial_{t_1} \boldsymbol{e}_k \mathrm{f}_k^{\mathrm{eq}} + \boldsymbol{e}_k \big(\boldsymbol{e}_k \nabla_1 \mathrm{f}_k^{\mathrm{eq}} \big) - \boldsymbol{e}_k F_k^{(1)} \big]. \tag{A7}$$

Summing Eqs. (A5)–(A7) over all subscripts k, the macroscopic conservation equations at t_1 and t_2 scales are

$$a_0 \partial_{t_1} I_{\mathrm{d}}^{\mathrm{m,n}} + \nabla_1 \big(\mathbf{u} I_{\mathrm{d}}^{\mathrm{m,n}} \big) = F^{(1)}, \tag{A8}$$

$$a_0 \partial_{t_2} I_{\mathrm{d}}^{\mathrm{m,n}} + \left(1 - \frac{\Delta t^*}{2\tau} \right) \nabla_1 \left\{ \sum_k \boldsymbol{e}_k \mathrm{f}_k^{(1)} \right\} + \frac{\Delta t^*}{2} \nabla_1 \left\{ \sum_k \boldsymbol{e}_k F_k^{(1)} \right\} = F^{(2)}, \tag{A9}$$

$$\sum_k \boldsymbol{e}_k \mathrm{f}_k^{(1)} = -\tau \left[\partial_{t_1} \big(\mathbf{u} I_{\mathrm{d}}^{\mathrm{m,n}} \big) + \nabla_1 \left\{ \sum_k \boldsymbol{e}_k \boldsymbol{e}_k \mathrm{f}_k^{\mathrm{eq}} \right\} - \sum_k \boldsymbol{e}_k F_k^{(1)} \right]. \tag{A10}$$

Using Eq. (16b), the quantity $\nabla_1 \{ \sum_k \boldsymbol{e}_k \boldsymbol{e}_k \mathrm{f}_k^{\mathrm{eq}} \}$ is expressed as

$$\nabla_1 \left\{ \sum_k \boldsymbol{e}_k \boldsymbol{e}_k \mathrm{f}_k^{\mathrm{eq}} \right\} = \nabla_1 \left\{ \frac{\mathbf{u}\mathbf{u}}{a_0} I_{\mathrm{d}}^{\mathrm{m,n}} \right\} = \mathbf{u}\mathbf{u} \left(\frac{a_0 \nabla_1 I_{\mathrm{d}}^{\mathrm{m,n}} - I_{\mathrm{d}}^{\mathrm{m,n}} \nabla_1 a_0}{a_0^2} \right) + \frac{I_{\mathrm{d}}^{\mathrm{m,n}}}{a_0} \underbrace{\nabla_1 (\mathbf{u}\mathbf{u})}_{\text{vector}}. \tag{A11}$$

After substitution of Eq. (A11) into Eq. (A10) and using Eq. (A2), it can be observed that

$$\sum_k \boldsymbol{e}_k \mathrm{f}_k^{(1)} = -\tau \left[\partial_{t_1}\left(\mathbf{u}I_\mathrm{d}^{\mathrm{m,n}}\right) + \mathbf{uu}\left(\frac{a_0 \nabla_1 I_\mathrm{d}^{\mathrm{m,n}} - I_\mathrm{d}^{\mathrm{m,n}}\nabla_1 a_0}{a_0^2} \right) + \frac{I_\mathrm{d}^{\mathrm{m,n}}}{a_0}\nabla_1(\mathbf{uu}) - \lambda\mathbf{u}\left(\frac{a_0 F^{(1)} - I_\mathrm{d}^{\mathrm{m,n}}(\mathbf{u}\cdot\nabla_1 a_0)}{a_0^2} \right) - \lambda_0 G_0^{(1)}\frac{\mathbf{u}}{a_0} \right]. \tag{A12}$$

Using Eq. (A8) to obtain $\partial_{t_1}(\mathbf{u}I_\mathrm{d}^{\mathrm{m,n}})$ and substituting into Eq. (A12) yields

$$\sum_k \boldsymbol{e}_k \mathrm{f}_k^{(1)} = -\tau \left[\mathbf{u}\frac{F^{(1)} - \nabla_1\left(\mathbf{u}I_\mathrm{d}^{\mathrm{m,n}}\right)}{a_0} + \mathbf{uu}\left(\frac{\nabla_1 I_\mathrm{d}^{\mathrm{m,n}}}{a_0} - \frac{I_\mathrm{d}^{\mathrm{m,n}}\nabla_1 a_0}{a_0^2} \right) \right.$$
$$\left. + \frac{I_\mathrm{d}^{\mathrm{m,n}}}{a_0}\nabla_1(\mathbf{uu}) - \lambda\mathbf{u}\left(\frac{a_0 F^{(1)} - I_\mathrm{d}^{\mathrm{m,n}}(\mathbf{u}\cdot\nabla_1 a_0)}{a_0^2} \right) - \lambda_0 G_0^{(1)}\frac{\mathbf{u}}{a_0} \right]. \tag{A13}$$

Using the mathematical formula $\mathbf{uu}(\nabla_1\psi) = \mathbf{u}\nabla_1(\mathbf{u}\psi) - \psi\,\mathbf{u}(\nabla_1\cdot\mathbf{u})$ in Appendix B, Eq. (A13) reduces to

$$\sum_k \boldsymbol{e}_k \mathrm{f}_k^{(1)} = \tau(\lambda-1)\mathbf{u}\left[\frac{F^{(1)}}{a_0} - I_\mathrm{d}^{\mathrm{m,n}}\frac{\mathbf{u}\cdot\nabla_1 a_0}{a_0^2} \right] - \tau\left[\frac{I_\mathrm{d}^{\mathrm{m,n}}}{n}\nabla_1(\mathbf{uu}) - \mathbf{u}I_\mathrm{d}^{\mathrm{m,n}}\frac{\nabla_1\cdot\mathbf{u}}{a_0} - \lambda_0 G_0^{(1)}\frac{\mathbf{u}}{a_0} \right]. \tag{A14}$$

Inserting Eq. (A14) into Eq. (A9), the results can be expressed as

$$a_0\partial_{t_2}I_\mathrm{d}^{\mathrm{m,n}} + \left(\tau - \frac{\Delta t^*}{2} - \lambda\tau \right)\nabla_1\left\{ I_\mathrm{d}^{\mathrm{m,n}}\mathbf{u}\left(\frac{\mathbf{u}\cdot\nabla_1 a_0}{a_0^2} \right) - \mathbf{u}\frac{F^{(1)}}{a_0} \right\}$$
$$+ \nabla_1\left\{ \lambda_0\tau G_0^{(1)}\frac{\mathbf{u}}{a_0} - \left(\tau - \frac{\Delta t^*}{2} \right)I_\mathrm{d}^{\mathrm{m,n}}\left[\frac{\nabla_1(\mathbf{uu})}{a_0} - \mathbf{u}\frac{\nabla_1\cdot\mathbf{u}}{a_0} \right] \right\} = F^{(2)}. \tag{A15}$$

Setting $\lambda = \lambda_0 = 1 - 0.5\Delta t^*/\tau$ and $G_0^{(1)}\mathbf{u} = I_\mathrm{d}^{\mathrm{m,n}}[\nabla_1(\mathbf{uu}) - \mathbf{u}(\nabla_1\cdot\mathbf{u})]$, Eq. (A15) reduces to

$$a_0\partial_{t_2}I_\mathrm{d}^{\mathrm{m,n}} = F^{(2)}. \tag{A16}$$

Combining $\varepsilon\times$ Eq. (A8) $+ \varepsilon^2\times$ Eq. (A16) yields

$$a_0\frac{\partial I_\mathrm{d}^{\mathrm{m,n}}}{\partial t^*} + \nabla^*\left(\mathbf{u}I_\mathrm{d}^{\mathrm{m,n}}\right) = F^{\mathrm{m,n}}. \tag{A17}$$

So, the partial source term G_0 is such that $G_0\mathbf{u} = I_\mathrm{d}^{\mathrm{m,n}}[\nabla^*(\mathbf{uu}) - \mathbf{u}(\nabla^*\cdot\mathbf{u})]$, and then

$$G_0 = I_\mathrm{d}^{\mathrm{m,n}}\left(\frac{\mathbf{u}\cdot\nabla^*(\mathbf{uu})}{|\mathbf{u}|^2} - \nabla^*\cdot\mathbf{u} \right). \tag{A18}$$

APPENDIX B: MATHEMATICAL FORMULAS USED FOR THE LBM

In this Appendix we present the following formulas, which are used for the LBM:

$$\mathbf{uu}(\nabla\psi) = \begin{pmatrix} \mathrm{u}_\mathrm{x}^2\nabla_\mathrm{x}\psi + \mathrm{u}_\mathrm{x}\mathrm{u}_\mathrm{y}\nabla_\mathrm{y}\psi \\ \mathrm{u}_\mathrm{x}\mathrm{u}_\mathrm{y}\nabla_\mathrm{x}\psi + \mathrm{u}_\mathrm{y}^2\nabla_\mathrm{y}\psi \end{pmatrix}, \tag{B1}$$

$$\mathbf{u}\nabla(\mathbf{u}\psi) = \begin{pmatrix} \mathrm{u}_\mathrm{x}^2\nabla_\mathrm{x}\psi + \mathrm{u}_\mathrm{x}\psi\nabla_\mathrm{x}\mathrm{u}_\mathrm{x} + \mathrm{u}_\mathrm{x}\mathrm{u}_\mathrm{y}\nabla_\mathrm{y}\psi + \mathrm{u}_\mathrm{x}\psi\nabla_\mathrm{y}\mathrm{u}_\mathrm{y} \\ \mathrm{u}_\mathrm{x}\mathrm{u}_\mathrm{y}\nabla_\mathrm{x}\psi + \mathrm{u}_\mathrm{y}\psi\nabla_\mathrm{x}\mathrm{u}_\mathrm{x} + \mathrm{u}_\mathrm{y}^2\nabla_\mathrm{y}\psi + \mathrm{u}_\mathrm{y}\psi\nabla_\mathrm{y}\mathrm{u}_\mathrm{y} \end{pmatrix}, \tag{B2}$$

$$\mathbf{uu}(\nabla\psi) - \mathbf{u}\nabla(\mathbf{u}\psi) = -\psi\begin{pmatrix} \mathrm{u}_\mathrm{x} \\ \mathrm{u}_\mathrm{y} \end{pmatrix}[\nabla_\mathrm{x}\mathrm{u}_\mathrm{x} + \nabla_\mathrm{y}\mathrm{u}_\mathrm{y}] = -\psi\,\mathbf{u}(\nabla\cdot\mathbf{u}), \tag{B3}$$

$$\nabla(\mathbf{uu}) = \begin{pmatrix} \nabla_\mathrm{x}(\mathrm{u}_\mathrm{x}\mathrm{u}_\mathrm{x}) + \nabla_\mathrm{y}(\mathrm{u}_\mathrm{x}\mathrm{u}_\mathrm{y}) \\ \nabla_\mathrm{x}(\mathrm{u}_\mathrm{x}\mathrm{u}_\mathrm{y}) + \nabla_\mathrm{y}(\mathrm{u}_\mathrm{y}\mathrm{u}_\mathrm{y}) \end{pmatrix}, \tag{B4}$$

$$\frac{\mathbf{u}\cdot\nabla(\mathbf{uu})}{|\mathbf{u}|^2} - \nabla\cdot\mathbf{u} = \frac{\mathrm{u}_\mathrm{x}^2\nabla_\mathrm{x}\mathrm{u}_\mathrm{x} + \mathrm{u}_\mathrm{y}^2\nabla_\mathrm{y}\mathrm{u}_\mathrm{y}}{\mathrm{u}_\mathrm{x}^2 + \mathrm{u}_\mathrm{y}^2} + \frac{\mathrm{u}_\mathrm{x}\mathrm{u}_\mathrm{y}\left(\nabla_\mathrm{x}\mathrm{u}_\mathrm{y} + \nabla_\mathrm{y}\mathrm{u}_\mathrm{x}\right)}{\mathrm{u}_\mathrm{x}^2 + \mathrm{u}_\mathrm{y}^2} \tag{B5}$$

[1] A. Liemert and A. Kienle, Analytical solution of the radiative transfer equation for infinite space fluence, Phys. Rev. A **83**, 015804 (2011).

[2] C.-H. Wang, Y.-Y. Feng, Y.-H. Yang, Y. Zhang, K. Yue, and X.-X. Zhang, Chebyshev collocation spectral method for

vector radiative transfer equation and its applications in two-layered media, J. Quant. Spectrosc. Radiat. Transf. **243**, 106822 (2020).

[3] A. Fokou, R. Tapimo, G. L. Ymeli, R. R Tchinda, and H. T. T. Kamdem, Radiation distribution in inhomogeneous

atmosphere-ocean system by discrete spherical harmonics method, J. Quant. Spectrosc. Radiat. Transf. **270**, 107707 (2021).

[4] J. J. Duderstadt and W. R. Martin, *Transport Theory* (Wiley, New York, 1979).

[5] E. W. Larsen, F. Malvagi, and G. C. Pomraning, One-dimensional models for neutral particle transport in ducts, Nucl. Sci. Eng. **93**, 13 (1986).

[6] R. D. M. Garcia, An analytical discrete-ordinates solution for an improved one-dimensional model of three-dimensional transport in ducts, Ann. Nucl. Energy **86**, 55 (2015).

[7] J. H. Randrianalisoa, L. A. Dombrovsky, W. Lipinski, and V. Timchenko, Effects of short pulsed laser radiation on transient heating of superficial human tissues, Int. J. Heat Mass Transf. **78**, 488 (2014).

[8] D. Baillis, R. Coquard, J. Randrianalisoa, L. Dombrovsky, and R. Viskanta, Thermal radiation properties of highly porous cellular foams, Spec. Top. Rev. Porous Media **4**, 111 (2013).

[9] R. Viskanta and M. P. Mengüç, Radiation heat transfer in combustion systems, Prog. Energy Combust. Sci. **13**, 97 (1987).

[10] H. Ebrahimi, A. Zamaniyan, J. S. S. Mohammadzadeh, and A. A. Khalili, Zonal modeling of radiative heat transfer in industrial furnaces using simplified model for exchange area calculation, Appl. Math. Model. **3**, 78004 (2013).

[11] J. M. Zhao and L. H. Liu, Radiative transfer equation and solutions, in *Handbook of Thermal Science and Engineering*, edited by F. Kulacki (Springer, 2017).

[12] S. Wen, H. Qi, Y.-R. Ren, J.-P. Sun, and L.-R. Ruan, Solution of inverse radiation-conduction problems using a Kalman filter coupled with the recursive least-square estimator, Int. J. Heat Mass Transf. **111**, 582 (2017).

[13] H. T. T. Kamdem, Ray effects elimination in discrete ordinates and finite volume methods, J. Thermophys. Heat Transf. **29**, 306 (2015).

[14] J. C. Chai, Transient radiative transfer in irregular two-dimensional geometries, J. Quant. Spectrosc. Radiat. Transf. **84**, 281 (2004).

[15] C.-H. Wang, Y. Zhang, H.-L. Yi, and H.-P. Tan, Transient radiative transfer in two-dimensional graded- index medium by Monte Carlo method combined with the time shift and superposition principle, Num. Heat Transf., Pt. A **69**, 574 (2016).

[16] L.-Y. Wei, H. Qi, Z.-T. Niu, Y.-T. Ren, and L.-M. Ruan, Reverse Monte Carlo coupled with Runge-Kutta ray tracing method for radiative heat transfer in graded-index media, Infr. Phys. Technol. **99**, 5 (2019).

[17] P. Ben-Abdallah and V. Le Dez, Temperature field inside an absorbing-emitting semitransparent slab at radiative equilibrium with variable spatial refractive index, J. Quant. Spectrosc. Radiat. Transf. **65**, 595 (2000).

[18] P. Ben-Abdallah, M. Sakami, V. Le Dez, and J. B. Saulnier, Two-dimensional analytical solutions of the radiative transfer equation for the axisymmetrical inhomogeneous semitransparent medium, CRAS-IIB **328**, 47 (2000).

[19] A. Dehghanian and S. M. H. Sarvari, Transient radiative transfer in variable index media using the discrete transfer method, J. Quant. Spectrosc. Radiat. Transf. **255**, 107259 (2020).

[20] Y. Sun, S. Li, R. Zhou, Z. Guo, and J. Ma, Spatial-angular spectral element method with discontinuous Galerkin schemes for radiative transfer in 2D irregular enclosures with obstacle

based on unstructured spatial elements, J. Quant. Spectrosc. Radiat. Transf. **280**, 108082 (2022).

[21] C.-A. Wang, H. Sadat, and V. Le Dez, Meshless method for solving multidimensional radiative transfer in graded index medium, Appl. Math. Modell. **36**, 5309 (2012).

[22] B. W. Webb, J. Ma, J. T. Pearson, and V. P. Solovjov, SLW modeling of radiation transfer in comprehensive combustion predictions, Combust. Sci. Technol. **190**, 1392 (2018).

[23] Y. Sun and X. Zhang, A hybrid strategy of lattice Boltzmann method and finite volume method for combined conduction and radiation in irregular geometry, Int. J. Heat Mass Transf. **121**, 1039 (2018).

[24] M. Abaszadeh, A. Safavinejad, H. Amiri, and A. A. Deloue, A direct–forcing IB–LBM implementation for thermal radiations in irregular geometries, J. Therm. Analys. Calorimetry **147**, 11169 (2022).

[25] M. Vajdi, F. S. Moghanlou, F. Sharifianjazi, M. S. Asl, and M. Shokouhimehr, A review on the Comsol Multiphysics studies of heat transfer in advanced ceramics, J. Compos. Comp. **2**, 35 (2020).

[26] C. Wang, T.-R. Shen, J. P. Gao, and J.-Y. Tan, Development of RTE solver for radiative transfer in absorbing–emitting medium using finite volume based CFD library OpenFoam, Int. J. Therm. Sci. **140**, 36 (2019).

[27] D. Y. Byun, S. W. Baek, and M. Y. Kim, Investigation of radiative heat transfer in complex geometries using blocked-off, multiblock and embedded boundary treatments, Num. Heat Transf., Pt. A **43**, 807 (2003).

[28] M. Mohammadi, S. Abdolreza, and G. Nassab, Application of the immersed boundary method in solution of radiative heat transfer problems, J. Quant. Spectrosc. Radiat. Transf. **260**, 107467 (2021).

[29] H. S. M. Sarvari, Solution of multi-dimensional radiative heat transfer in graded index media using the discrete transfer method, Int. J. Heat and Mass Transfer **112**, 1098 (2017).

[30] Y.-Y. Feng and C. H. Wang, Discontinuous finite element method applied to transient pure and coupled radiative heat transfer, Int. Commun. Heat Mass Transf. **122**, 105156 (2021).

[31] R.-R. Zhou and B.-W. Li, The modified discrete ordinates method for radiative heat transfer in two-dimensional cylindrical medium, Int. J. Heat Mass Transf. **139**, 1018 (2019).

[32] C. K. Aidun and J. R. Clausen, Lattice-Boltzmann method for complex flows, Ann. Rev. Fluid Mech. **42**, 439 (2010).

[33] Y. Wang, L. Yan, and Y. Ma, Lattice Boltzmann solution of the transient Boltzmann transport equation in radiative and neutron transport, Phys. Rev. E **95**, 063313 (2017).

[34] H. L. Yi, F. J. Yao, and H. P. Tan, Lattice Boltzmann model for a steady radiative transfer equation, Phys. Rev. E **94**, 023312 (2016).

[35] X. Liu, Y. Huang, C.-H. Wang, and K. Zhu, Solving steady and transient radiative transfer problems with strong inhomogeneity via a lattice Boltzmann method, Int. J. Heat Mass Transf. **155**, 119714 (2020).

[36] X. Liu, Y. Huang, C.-H. Wang, and Z. Zhu, A multiple-relaxation–time lattice Boltzmann model for radiative transfer equation, J. Computat. Phys. **429**, 110007 (2020).

[37] X. Liu, H. Wu, K. Zhu, and Y. Huang, Lattice Boltzmann model for multidimensional polarized radiative transfer: Theory and application, Optica **8**, 1136 (2021).

[38] Y. Zhang, H.-L. Yi, and H.-P. Tan, Lattice Boltzmann method for short-pulsed laser transport in a multi-layered medium, J. Quant. Spectrosc. Radiat. Transf. **155**, 75 (2015).

[39] Y.-H. Wang, L.-M. Yan, B.-Y. Xia, and Y. Ma, Lattice Boltzmann method for simulation of time-dependent neutral particle transport, Nucl. Sci. Tech. **28**, 36 (2017).

[40] X. Liu, S. Wu, K. Zhu, Y. Cai, and Y. Huang, Mesoscopic lattice Boltzmann model for radiative heat transfer in graded-index media, Phys. Rev. Res. **4**, 013125 (2022).

[41] S. B. Mansoor, Computational aspect of radiative transfer equation in non–orthogonal coordinates, J. Thermal Eng. **5**, 162 (2019).

[42] Y. Zhang, H.-L. Yi, and H.-P. Tan, Analysis of transient radiative transfer in two-dimensional scattering graded index medium with diffuse energy pulse irradiation, Int. J. Thermal Sci. **87**, 187 (2015).

[43] M. Sakami, K. Mitra, and P.-F. Hsu, Analysis of light pulse transport through two-dimensional scattering and absorbing media, J. Quant. Spectrosc. Radiat. Transf. **73**, 169 (2002).

[44] Y. Zhang, H.-L. Yi, M. Xie, and H.-P. Tan, Short-pulsed laser transport in two-dimensional scattering media by natural element method, J. Opt. Soc. Am. A **31**, 818 (2014).

[45] Y. Wang, M. Xie, and Y. Ma, Neutron transport solution of lattice Boltzmann method and streaming-based block-structured adaptive mesh refinement, Ann. Nucl. Energ. **118**, 249 (2018).

[46] B. Shi and Z. Guo, Lattice Boltzmann model for nonlinear convection-diffusion equations, Phys. Rev. E **79**, 016701 (2009).

[47] X. He and G. Doolen, Lattice Boltzmann method on curvilinear system: Flow around a circular cylinder, J. Computat. Phys. **134**, 306 (1997).

[48] Q. Li, Y. L. He, and Y. J. Gao, Implementation of finite–difference lattice Boltzmann method on general body–fitted curvilinear coordinates, Int. J. Mod. Phys. **19**, 1581 (2008).

[49] J. A. R. Barraza and R. Deiterding, A lattice Boltzmann method in generalized curvilinear coordinates, *VI International Conference on Particle-based Method—Fundamentals and Applications* (Particles, 2019), pp. 477–488.

[50] A. A. Mohammad, *Lattice Boltzmann Method, Fundamentals and Engineering Applications with Computer Codes*, 2nd ed. (Springer-Verlag, London, 2019).

[51] L. G. Zhao, Z. Chu-Guang, and S. Bao-Chang, Non-equilibrium extrapolation method for velocity and pressure boundary conditions in the lattice Boltzmann method, Chin. Phys. **11**, 366 (2002).

[52] L. H. Liu and P.-F. Hsu, Analysis of transient radiative transfer in semitransparent graded index medium, J. Quant. Spectrosc. Radiat. Transf. **105**, 357 (2007).

[53] J. M. Zhao and L. H. Liu, Least-squares spectral element method for radiative heat transfer in semitransparent media, Numer. Heat Transf., Pt. B **50**, 473 (2006).

[54] T.-K. Kim and H. Lee, Effect of anisotropic scattering on radiative heat transfer in two-dimensional rectangular enclosures, Int. J. Heat Mass Transf. **31**, 1711 (1988).

[55] W. A. Fiveland and J. P. Jessee, Finite element formulation of the discrete-ordinates method for multidimensional geometries, J. Thermophys. Heat Transf. **8**, 426 (1994).

[56] S. C. Mishra, P. Talukdar, D. Trimis, and F. Durst, Computational efficiency improvements of the radiative transfer problems with or without conduction–A comparison of the collapsed dimension method and the discrete transfer method, Int. J. Heat Mass Transf. **46**, 3083 (2003).

[57] L. H. Liu, Benchmark numerical solutions for radiative heat transfer in two-dimensional medium with graded index distribution, J. Quant. Spectrosc. Radiat. Transf. **102**, 293 (2006).

[58] L. H. Liu and L. J. Liu, Discontinuous finite element method for radiative heat transfer in semitransparent graded index medium, J. Quant. Spectrosc. Radiat. Transf. **105**, 377 (2007).

[59] L. H. Liu, L. Zhang, and H. P. Tan, Finite element method for radiation heat transfer in multi-dimensional graded index medium, J. Quant. Spectrosc. Radiat. Transf. **97**, 436 (2006).

[60] J. M. Zhao and L. H. Liu, Solution of radiative heat transfer in graded index media by least square spectral element method, Int. J. Heat Mass Transf. **50**, 2634 (2007).

[61] A.-S. W. Lindberg, T. M. Jorgensen, and V. A. Dahl, Interpolation from grid lines: Transfinite and weighted method, in *Image Analysis*, *Lecture Notes in Computer Science No. 10270* (Springer, 2017), pp. 338–349.

[62] J. C. Chai and G. Parthasarathy, Finite volume radiative heat transfer procedure for irregular geometries, J. Thermophys. Heat Transf. **9**, 410 (1995).

[63] D. Y. Byun, S. W. Baek, and M. Y. Kim, Thermal radiation in a discretely heated irregular geometry using the Monte-Carlo, finite volume, and modified discrete ordinates interpolation method, Numer. Heat Transf., Pt. A **37**, 1 (2000).

[64] J. R. Howell and M. P. Mengüç, Challenges for radiative transfer 1: Towards the effective solution of conjugate heat transfer problems, J. Quant. Spectrosc. Radiat. Transf. **221**, 253 (2018).